[ChNum] 19

[ChTitle] Non-linear Spectroscopies

[Authors] Juliana Cuéllar-Zuquin, Angelo Giussani and Javier Segarra-Martí

[Author Affiliaton(s)] Instituto de Ciencia Molecular, Universitat de València, C/ Catedrático José Beltrán nº 2, 46980 Paterna, Valencia, Spain

[NON PRINT ITEMS]

Abstract: In this chapter we cover in detail the connections between electronic structure theory and the experimental observables registered in linear and non-linear optical spectroscopic set-ups. The main goal is to show different approaches of increasing complexity to model optical spectra and their lineshapes for both steady state (linear) and time-resolved (pump-probe and two-Dimensional Electronic Spectroscopy, 2DES) variants, and how these models can offer a more detailed characterisation of a system's photo-response. We start with a brief introduction to Liouville space, and how the density matrix and its evolution can be used to express the different light-matter interactions occurring in linear and non-linear optical experiments. We then introduce the sum-over-states approach and point out the connection between the density matrix and the transition energies and transition dipole moments obtained from electronic structure theory codes. Lineshape broadenings are then defined semi-classically within the cumulant expansion of Gaussian fluctuations to second-order, outlining the displaced Brownian oscillator model and the basic theory behind lineshape functions. We show different approximations in linear and non-linear spectra, and for both steady-state and time-resolved situations, highlighting strengths and weaknesses through their application to a series of different molecular systems. We attempt to provide guidelines for specific

cases where the different approaches might be appropriate, aiming to outline their range of applicability.

Keywords:

Absorption; theoretical spectroscopy; non-linear spectroscopy; 2DES; pump-probe; CASSCF/CASPT2; electronic structure theory; Liouville space; displaced Brownian oscillator

[Chapter Starts Here]

[19.1 Introduction]

Spectroscopy studies the interaction between radiation and matter.[1] In its simplest form, radiation (of varying wavelengths) is supplied to a sample, triggering well-known outcomes: the absorption of a photon, or the emission of a photon with different wavelengths from those initially absorbed, and that can occur within spontaneous and/or stimulated mechanisms. These underpin linear spectroscopies, which reflect the absorption and emission features, occur at the sample's absorbing ground state or equilibrium structure, often referred to as the Franck-Condon (FC) region.

Absorption and emission features of chemical compounds change depending on the radiation wavelength used: microwaves (MW) promote rovibrational excitations, infrared (IR) radiation populates vibrational energy levels, ultraviolet (UV)/visible (Vis) light facilitates electronic promotions, vacuum/extreme UV (VUV/XUV) trigger ionisations in the close-lying valence shell and X-rays access and eject the electrons in the inner electronic shells of molecules prompting core excitations/ionisations. Radiation therefore initiates different processes depending on the energy supplied to the system, triggering populations of different kinds of states (i.e. vibrational, electronic, …), and leading to distinct signals which depend strongly on the molecular structure of a given chemical compound and that are used for their characterisation. An exhaustive explanation of the photophysics and photochemistry fundamentals can be found in the first two chapters of this book.

Spectroscopy is widely used across multiple disciplines to characterise chemical species as well as to monitor their reactivity. Depending on the molecular process of interest, different radiation wavelengths may be used offering complementary information on a given compound: nuclear motion may be monitored by measuring IR vibrations activated during a given reaction,[2,3] electronic states can be probed to identify the active electronic state driving a photo-reaction,[4,5] and core excitations enable atom-specific probes of the electronic environment within a molecule and the solvent/environment in which they are embedded. From an experimental standpoint, this needs different radiation sources that use different set-ups and sometimes require the use of large-scale facilities; from a theoretical

side, however, it refers mostly (to some degree of approximation) to modelling different energy gaps and transition dipole moments depending on the specific kind of state populated by the radiation used, which can often be obtained from standard electronic structure packages at different levels of theory.

Our main goal in this chapter is to show different strategies to connect these two often-separated branches within the optical (electronic) domain: how do we get from the magnitudes estimated by theory to the experimental observables? And how are they actually related to one another? Experiments record signals like extinction coefficients or (non-linear) induced polarisabilities which lead to broad curves, while theory in its crudest form provides a simple stick at a given wavelength, where its associated intensity is approximated by computing the oscillator strength of a given transition. Elaborate theoretical models can move away from this simple stick representation by adding complexity in terms of spectral broadenings and line shapes that arise due to nuclear relaxation, non-adiabatic effects/finite lifetime or solvation. Such models connect more faithfully with experiment and enable the description of complex events like vibrational/vibronic coherent motion or excitation energy transfer,[6] whose interpretation relies not only on the wavelength and timescales in which associated peaks to these processes emerge but also with the concrete way spectral line shapes broaden over time.

While most of the above apply to steady-state (i.e., non time-resolved) situations, when studying excited state processes such as those widely featured in photochemistry, different needs have to be met: excited state dynamics tend to be short-lived and can simultaneously feature on multiple accessible states each with distinct reactivity, requiring a temporally resolved mapping of the excited state signals recorded. This leads to the use of more sophisticated set-ups that give access to non-linear optical properties, which map higher-order response signals. We focus on reviewing models to simulate optical 3rd order non-linear response contributions which underpin most experiments currently used in the literature like pump-probe or transient absorption. These techniques are known as non-linear spectroscopies, and by using a controlled sequence of laser pulses on the sample they record a temporally-resolved signal that measures state or reaction lifetimes and thus keeps track of the pace at which a given reaction takes place.

The development of non-linear spectroscopies was mostly driven in the 70s and 80s with the goal of observing how chemical reactions occur in real time.[7] This was accomplished by Zewail and co-workers in the late 80s, warranting the Nobel Prize in Chemistry in 1999, and represents one of the so-called "Holy Grails" in Chemistry of observing chemical reactions as they happen.[8] Observing nuclear motion in real time was a fundamental step to further understand chemical reactivity, as it allowed also the isolation and characterisation of elusive reactive (intermediate) structures like transition states.[9] This milestone gave birth to the field of *femtochemistry*,[10] which refers to the specific area of physical chemistry (or photochemistry) studying chemical reactions on the femtosecond (fs, i.e., 10^{-15} s) timescale and enabling the observation of nuclear motion, i.e., the rearrangement of atoms in molecules forming new molecules or products that is at the root of chemical reactivity.

When used with high-energy and/or strong-field (ionising) radiation, spectroscopy can measure the ionisation of the sample instead of its absorption, leading to complementary signals arising from the transient cationic (normally doublet) species and the ejected electrons created. This is known as photoelectron spectroscopy,[11] and its signals are underpinned by a different set of rules to those governing excitation, which offers a different window to probe processes that may otherwise be optically dark and thus obscured. Photoelectron spectra can also be recorded in a time-resolved fashion,[12,13] and has recently gained importance as photoionisation is simultaneously sensitive to both electronic and nuclear components of a wave packet in a molecule.[12]

Recent advances in instrumentation through the advent of broadband ultrashort femtosecond light sources has enabled more complex set-ups to be built, which give access to new information on photophysical and photochemical mechanisms. A particularly relevant example is two-Dimensional Electronic Spectroscopy (2DES), which is a 3rd order optical non-linear response experiment with expanded resolution that is able to register couplings between chromophores and to measure coherences.[14–19] This technique has been widely used in the Vis window to study light-harvesting complexes and monitor their "wave-like" energy transfer,[20,21] which was initially believed to be rooted on electronic coherences. The additional excitation dimension enables observing off-diagonal peaks coupling different states and that can be used to monitor energy transfer. This extra dimension also provides a way to disentangle homogeneous and inhomogeneous broadening sources, which allows a better understanding of environmental effects, a crucial aspect in photoinduced biological processes embedded in the cellular media.

In this chapter we cover different computational strategies that use routine electronic structure data to build models which connect to experimentally registered optical spectroscopic observables. Different degrees of approximation are applied that modulate the trade-off between accuracy and computational cost/complexity sought, and where we analyse both their strengths as well as their limitations. We outline simple modelling tools to establish seamless connections between theory and experiment, helping assign, support and sometimes even predict steady-state and time-resolved spectral signals. This provides a molecular route map on how spectral signals might be interpreted: we aim to show how even the most qualitative models can often offer valuable state-to-signal assignments, connecting concrete molecular motions/features with experimentally recorded evidence, and enabling a more complete understanding of a photo-process.

The chapter is organised as follows: we start with a brief review of basic concepts to build spectral response functions, and then move onto applying these foundations to linear absorption, which stands as the base technique which will be built upon when devising more complex and time-resolved models. Non-linear spectra follow, looking particularly at ways to simulate pump-probe spectroscopy and briefly introduce 2DES, a novel technique that offers improved temporal and spectral resolution in the optical UV/Vis regime: we build upon the similarities between 2DES and pump-probe spectroscopy, highlighting the additional information provided in the more complex 2DES experiments, and lay out different approaches to model and help interpret these intricate spectral signals. We conclude by outlining the domains where the different methods work in

reproducing/interpreting experiment, aiming to guide the reader in the different approximations introduced and their range of applicability.

[19.2 Basic Concepts]

[19.2.1 Introduction to the Liouville space]

Some of the methods introduced below are framed within a Liouville space formulation, which might be unfamiliar. A very brief and simplified overview is laid out to provide basic tools to qualitatively understand the underlying physical processes behind the equations. A thorough description of the Liouville space, its properties and a detailed description of how the equations are derived can be found elsewhere.[22,23]

The Liouville space refers to the space of operators on Hilbert space. This means instead of describing properties in terms of wave functions for each individual molecule in our system, they are described in terms of a density matrix, which conveniently averages ensembles of molecules as those measured in spectroscopy. In the Liouville space, the interest lies in the temporal evolution of the density matrix representing our system of interest being measured. This density matrix operator can be defined as

$$\hat{\rho} = \sum_{ab} \rho_{ab} |a\rangle\langle b| \qquad (1)$$

where *a* and *b* run over the different electronic ground/excited states of the system. The definition of system is in principle quite broad: it may entail a single molecule and all (or some) of its electronic states, or larger macromolecules with several states per monomer. For the sake of simplicity, we will be focusing on monomers.

The density matrix operator $\hat{\rho}$ essentially has two types of terms: diagonal ($a=b$), and off-diagonal ($a \neq b$). Diagonal terms are called populations, while off-diagonal terms are referred to as coherences. Populations refer to the different electronic eigenstates of the system being formed or populated due to the action of the laser pulse sequence; coherences, on the other hand, are terms of the density matrix that couple states to one another.

The density matrix interacts with incoming light sources through the dipole operator $\hat{\mu}$,

$$\hat{\mu} = \sum_{ab} \mu_{ab} |a\rangle\langle b| \qquad (2)$$

where μ_{ab} is the transition dipole between states *a* and *b*. In the absence of an electric field, the system's Hamiltonian can be assumed to be formed by the eigenvalues of the molecular system under study, and the time evolution of the unperturbed density $\hat{\rho}^{(0)}(t) = \hat{\rho}_0$, i.e., the density of the ground state in equilibrium, can be described with the Liouville-von Neumann equation. Inclusion of a (weak) external field can be done perturbatively (see chapter 7 for light-matter strong field interactions), where the time-dependent perturbation to the Hamiltonian $H'(t)$ can be written as

$$\hat{H}'(t) = -\hat{\mu} \cdot E(t) \qquad (3)$$

where $E(t)$ refers to a time-dependent electric field (i.e., a laser pulse for example) and this perturbation is inserted in the Hamiltonian as $\hat{H}(t) = \hat{H}_0 + \hat{H}'(t)$, which implies dipole interactions between the sample and the incoming laser pulses.

The signal recorded in both linear and non-linear optical spectroscopic experiments (pump-probe and 2DES) can be framed in terms of the induced nonlinear polarisation, which is defined as the expectation value of the dipole operator $\hat{\mu}$ leading to:

$$P^{(n)}(t) = \langle \hat{\mu}\hat{\rho}^{(n)}(t) \rangle = Tr\left[\hat{\mu}\hat{\rho}^{(n)}(t)\right] \qquad (4)$$

where $\hat{\rho}(t)$ is the density matrix operator defined above and $P^{(n)}(t)$ is the general induced polarisation to nth order, which accounts for the subsequent laser (dipole) interactions $\hat{\mu}$ on the initial unperturbed density thus becoming then time-dependent. We remind that $Tr\left[\hat{\mu}\hat{\rho}^{(n)}(t)\right]$ refers to the trace, i.e., the sum of elements on the main diagonal of the square matrix $\left[\hat{\mu}\hat{\rho}^{(n)}(t)\right]$.

Over the next sections we build upon the basic concepts covered here to describe both linear and non-linear spectroscopies and the associated response signals measured on the system. Perhaps the most basic (and obvious) distinction to make between these two techniques upfront is that in linear spectroscopy the response of the system is linearly proportional to the incident field, while in non-linear spectroscopies it is not.

A detailed view on the explicit derivation of the complex working equations can be found elsewhere:[22,23] there are different approaches in the literature such as those based on the Liouville space and the Sum-Over-States (SOS) approach,[23,24] the Non-linear Exciton Propagation[25,26] or the Doorway-Window representation[27,28] just to name a few. Here we focus on the more practical aspects needed for simulating (to different degrees of approximation) linear and non-linear optical spectral signals using electronic structure data coupled to the SOS approach.[14,19,24,29]

[19.2.2 The displaced Brownian oscillator model]

A strategy to represent semi-classically lineshape broadenings is that of the Displaced Brownian Oscillator (DBO) model. To solve $P^{(n)}(t)$ we can use knowledge from electronic structure theory: in principle this can be solved without further approximations, if we were to know the evolution of the density matrix. This however requires propagating both populations and coherences (see section 2.1); the former has been treated with relative success semi-classically with a wide range of methods such as surface hopping[30–32] or multiple spawning,[33] but the latter requires more sophisticated quantum dynamics schemes[34,35] that can describe both quantum cross- and auto-correlation fluctuation functions[36–38] for the different density matrix terms (or states within the SOS approach[23,24]).

As quantum dynamics are out of reach for most applications, we focus on semi-classical approaches, and particularly on the stochastic modelling of bath fluctuations or stochastic Liouville equations.[39] In the stochastic Liouville equations, the response function is averaged over an ensemble of trajectories, propagated with molecular dynamics techniques, and where at subsequent timesteps $R^{(n)}(t)$, the nth order response signal $P^{(n)}(t)$ depends on, is evaluated. In this method, the Hamiltonian is formally time-independent but depends on a classical time-dependent stochastic variable which accounts for the bath (i.e. the solvent or intramolecular vibrations),[39] and (bulk)-bath dephasing effects are included through ensemble averaging. Several methods have been developed over the years in this direction, where the biggest hurdle is the computational cost of running swarms of (ground and/or electronic excited state) trajectories and the inclusion of quantum feedback on the classical bath during coherent state evolution.[25,27,40–45]

For systems that behave according to Gaussian statistic distributions and feature linear system-bath couplings, $R^{(n)}(t)$ can be solved using the second-order Cumulant expansion of Gaussian Fluctuations (CGF):[22,46,47] this method allows calculating electronic transition band shapes coupled to a bath fluctuating at arbitrary timescales through the formalism of line shape functions $g_{ab}(t)$.[19,37,48] Within the second-order CGF, different models can be employed which consider different number of partaking states: we focus on the Brownian oscillator model, which can be formulated in non-damped,[48] (over or under)damped,[23,49–51] or generalised[36] formulations. CGF can also be truncated to higher order (3rd order) terms, which appear to be important for systems embedded in polarisable baths[36,52] but that is not exact and thus would require higher order terms to verify convergence.[52] The most important aspect of the cumulant expansion is that it allows calculating the necessary (auto/cross)correlation functions without having to calculate the nuclear eigenstates,[22,46] i.e. it provides a semi-classical solution for the energy gap fluctuation functions which we can then obtain from electronic structure data.

This approximation allows obtaining analytical (i.e. exact within the 2nd order CGF) expressions for the lineshape functions $g_{ab}(t)$, which depend on the spectral density $J_{ab}(\omega)$ in the frequency domain, that is defined as

$$J_{ab}(\omega) = f(\omega,\beta)\int_{-\infty}^{\infty} C_{ab}(t)e^{i\omega t}dt \qquad (5)$$

where $f(\omega,\beta)$ is a pre-factor that accounts for the quantum to classical transformation. This magnitude accounts for the time-dependence of the electronic energy gap, which contains most of the required information to model optical spectral lineshapes. The spectral density in turn depends on $C_{ab}(t)$, which is the autocorrelation function of bath fluctuations, which is described in more detail later on in eq. 9.

The lineshape functions $g_{ab}(t)$ then read

$$g_{ab}(t) = -\frac{1}{2\pi}\int_0^{+\infty} d\omega \frac{J_{ab}(\omega)}{\omega^2}\left[coth\left(\frac{\beta\omega}{2}\right)(1-cos(\omega t)) + i(sin(\omega t) - \omega t)\right] \qquad (6)$$

where the temperature dependence is included within $\beta = 1/k_B T$. $C_{ab}(t)$ refers to the (auto/cross)-correlation function of the electronic energy gap and is the key quantity that carries all the microscopic information necessary for calculating the optical response functions within CGF to 2nd order.[22,46]

Assuming our system is coupled to a set of high-frequency (intramolecular) modes and a continuum of low-frequency (inter- and intramolecular) modes, the spectral density $J_{ab}(\omega)$ can be partitioned in: i) weakly undamped/underdamped contributions arising from the slowly decaying $C_{ab}(t)$ and related to high-frequency modes, which embody the vibrational progressions in the spectra, and ii) overdamped contributions from fast decaying $C_{ab}(t)$ associated with low-frequency modes that give rise to the homogeneous broadening of the signal.

The total lineshape function can therefore be represented as a sum of two parts: an underdamped part with the high-frequency responsible for vibrational progressions and an overdamped one embodying the low-frequency modes.[53] Within the high-temperature limit, the lineshape of the semi-classical overdamped regime can be represented as

$$g_{ab}^{OBO}(t) = \frac{\lambda_{ab}}{\Lambda}\left(\frac{2k_B T}{\hbar\Lambda} - i\right)(e^{-\Lambda t} + \Lambda t - 1) \qquad (7)$$

where λ_{ab} and Λ^{-1} are the system-bath coupling strength (also known as reorganisation energy) and fluctuation time scale, respectively. The former can be obtained from the molecular Hessian as outlined below, whereas the latter can be estimated either from molecular dynamics or from experiments.

Undamped vibrations are described within the (uncoupled) displaced Brownian harmonic oscillator

$$g_{ab}(t) = \sum_k \frac{\omega_k \tilde{d}_{ak}\tilde{d}_{bk}}{2}\left[coth\left(\frac{\omega_k}{2k_B T}\right)\left(1-cos(\omega_k t)\right) + i\, sin(\omega_k t)\right] \qquad (8)$$

which develops eq. 6 as a sum over the k normal modes of the molecule with ω_k frequency and where $\tilde{d}_{ak}$ is the displacement of the a^{th} electronic potential along the k^{th} mass-weighted normal mode (see Fig. 1).[49,54]

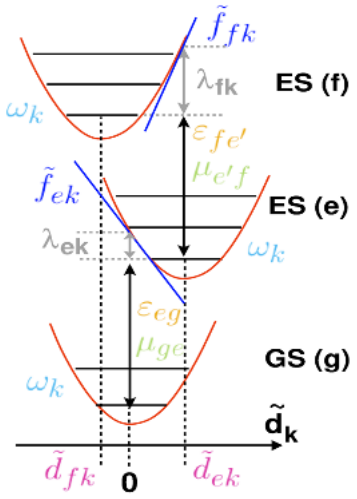

Figure 1. Diagram of a displaced harmonic oscillator model for a three-level system: g represents the electronic ground state, e denotes the populated electronic states after the pump sequence and f refers to the higher-lying excited states accessed in excited state absorptions from states e. Reproduced from ref. 49 with permission from the American Chemical Society.

The DBO model allows displacing the normal modes computed for the ground state to the rest of the electronic excited states considered: as shown in Fig. 1 displacement vectors $\tilde{d}_{ak}$ ($\tilde{d}_{ek}$for state e and $\tilde{d}_{fk}$ for state f in this case) are associated with two transitions and depend on cross-correlation functions $C_{ab}(\omega)$ where $a \neq b$.

From a practical standpoint, this requires computing the ground state Hessian and its frequencies ω_k, as well as the gradients of all excited states considered ($\tilde{f}_{ek}/\tilde{f}_{fk}$) to obtain the displacement vectors ($\tilde{d}_{ek}/\tilde{d}_{fk}$) to project the ground state Hessian onto the excited states e and f.[49,54] This adds excited state gradients and the ground state Hessian to the energies and transition dipoles already required between each electronic state for this type of calculation, which allows also obtaining the so-called reorganisation energies ($\lambda_{ek}/\lambda_{fk}$) that are widely used in Marcus' theory for electron transfer,[55] for example. It should be noted that one can directly compute the excited state Hessians and account for Duschinsky rotations instead of relying on displacements:[52] this is however computationally expensive as it requires optimising and obtaining Hessians for each and every different electronic state in the model.

[19.2.3 Including solvent effects through energy gap correlation functions]

To include the energy fluctuations due to solute-solvent interactions different approaches have been developed. A more straight-forward way for obtaining the spectral density $J_{ab}(\omega)$ is to evaluate it directly from the (auto/cross)-correlation functions by extracting the energy gap time-dependence and Fourier-transforming it to the frequency domain (using eq. 5) by evaluating the following expression

$$C_{ab}(t) = \left\langle (\delta\varepsilon_{ga}(t) - \delta\bar{\varepsilon}_{ga})(\delta\varepsilon_{gb}(0) - \delta\bar{\varepsilon}_{gb}) \right\rangle \qquad (9)$$

where $\bar{\varepsilon}_{ga}$ is the average energy along the time-dependent fluctuations $\delta\varepsilon_{ga}(t)$.

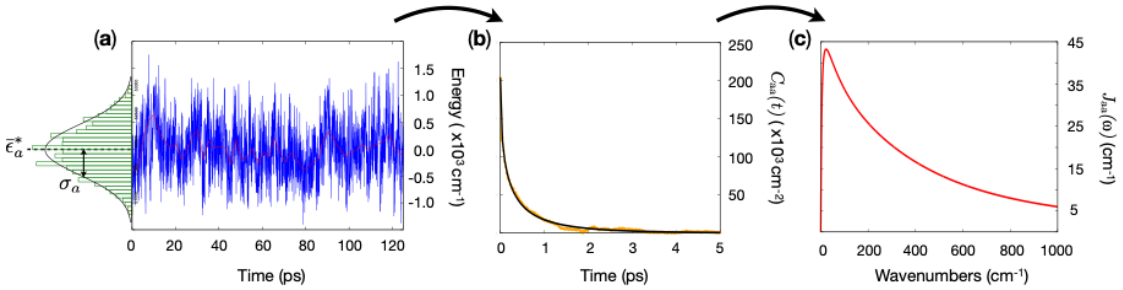

Figure 2. From the fluctuating energy gap (a), through the gap fluctuation autocorrelation function $C_{aa}(t)$ (b) and the static disorder energy distribution (on the side of (a)), to the spectral density $J_{aa}(\omega)$ (c). $C_{aa}(t)$ is fitted by a stretched exponential (black line in (b)), while the static disorder is fitted by a Gaussian function ($\bar{\varepsilon}_a^*, \sigma_a$). Reproduced from Ref. 37, with permission from the Royal Society of Chemistry.

Fig. 2 shows a brief scheme of how this can be technically done: one needs to compute the energy gap between states along an MD trajectory (Fig. 2a), which may be obtained using quantum mechanical[56,57] or semi-classical methods,[37,58,59] and which can be used to build the (auto/cross)-correlation function. This correlation function (Fig. 2b) can then be damped[60] to ensure decay and be fitted to a stretched exponential, $f_{\tau,\beta}(t) = exp\left[-(t/\tau)^{\beta}\right]$,[37] which smoothens the function to be subsequently Fourier transformed (Fig. 2c).

Solvent fluctuations around the solute lead to different nuclear (or solvent) configurations and to a time-dependent energy gap fluctuation which gives rise to dynamic disorder. Static disorder, on the other hand, is obtained by building a distribution of excitation energies for each state a, which can be fitted to a Gaussian function: the centre of the Gaussian is the average transition energy along the trajectory ($\bar{\varepsilon}_a^*$), while its width (σ_a) describes how broad is the excitation energy distribution and is referred to as the static disorder.

From this one can obtain the spectral density for any arbitrary state (i.e. $C_{ab}(t)$ where $a = b$), and also the cross-correlation terms (i.e. $C_{ab}(t)$ where $a \neq b$) which are often neglected but that are important for describing non-linear spectroscopic lineshapes.[37]

[19.3 Linear Absorption]

The first of the spectroscopies covered is linear absorption, which stands as the simplest technique to build upon when formulating complex non-linear experiments. In linear absorption, a sample (i.e., a molecular system in our case) is exposed to radiation, which triggers the population of one or more electronic excited states resonant with the incident radiation wavelength.

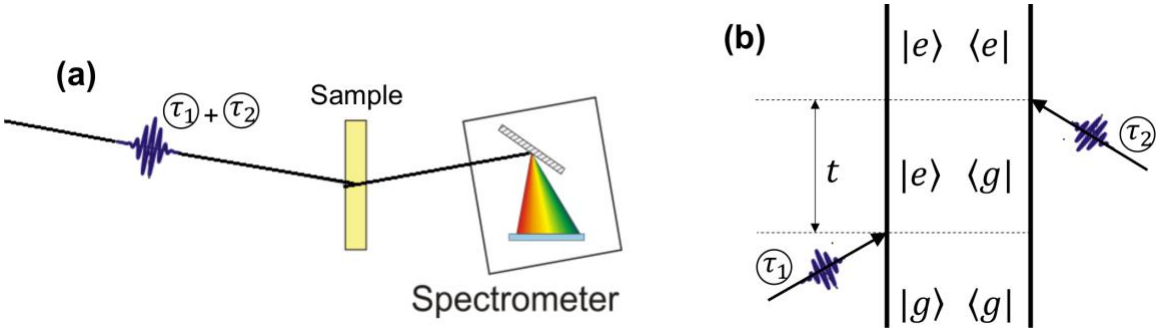

Figure 3. Scheme of a linear absorption experiment (a) and the double-sided Feynman interaction diagram representing absorption (b).

A schematic representation of a standard linear absorption experiment is shown in Fig. 3a. Theoretically, linear absorption can be seen as two sequential light-matter interactions which can be represented with a double-sided Feynman diagram (Fig. 3b): the first photon creates a coherent state eg (see Section 2.1), while the second photon arrives after time t and creates the population of the electronic excited state e (i.e. the population ρ_{ee}). Fourier-transforming over this time t leads to the spectrum in the frequency domain, which is the one often presented in the literature.

We restrict ourselves to absorption features: the methods described in this section can also be formulated to describe steady-state emission spectra which would correspond to outgoing photons starting from the excited state e (i.e. the ee element of $\hat{\rho}$ in Fig. 3b) with different degrees of complexity, but are left out for the sake of simplicity.

[19.3.1 Linear spectroscopy in the Liouville Space]

Within 1st-order, which refers to linear absorption, the induced polarisability $P^{(n)}(t)$ can be defined as

$$P^{(1)}(t) = \langle \hat{\mu}\hat{\rho}^{(1)}(t) \rangle = \int_0^\infty dt_1 R^{(1)}(t_1) \times E(t - t_1) \qquad (10)$$

where $R^{(1)}(t_1)$ is the 1st-order response function and $E(t-t_1)$ denotes the incident radiation source. $R^{(1)}(t_1)$ can be further developed as

$$R^{(1)}(t_1) = \left(\frac{i}{\hbar}\right) Tr\left[\hat{\mu}\mathbb{G}(t_1)[\hat{\mu}, \hat{\rho}_0]\right] \qquad (11)$$

and where $\hat{\rho}_0$ is the unperturbed density matrix (i.e. the ground state density prior to any light-matter interaction) and $\mathbb{G}(t_1)$ is the retarded Green's function describing the density matrix evolution in the absence of an external field.[22,29] Within the SOS approach this can be expanded in terms of the system's eigenstates, leading to

$$R^{(1)}(t_1) = \left(\frac{i}{\hbar}\right) \Theta(t_1) \sum_e \left|\mu_{eg}\right|^2 e^{-i(\omega_{eg} - i\gamma_{eg})t_1} \qquad (12)$$

where $\Theta(t_1)$ is the Heaviside function ensuring causality, μ_{eg} refers to the associated transition dipole moment, ω_{eg} to the transition energy (i.e. coherence terms of $\hat{\rho}$ where $a \neq b$) and γ_{eg} is a dephasing rate which accounts for the coherence decay between the electronic states e and g. γ_{eg} originates due to a number of factors: pure dephasing or internal conversion amongst others.[29] By Fourier-transforming and extracting the real (absorptive) part of the expression above we obtain

$$P^{(1)}(\Omega) = \sum_e \frac{|\mu_{eg}|^2}{\Omega - \omega_{eg} + i\gamma_{eg}} \qquad (13)$$

which represents a sum of Lorentzian contributions centred at ω_{eg} to the absorption, with their widths being influenced by the dephasing rate γ_{eg}.[22] This simplified expression, where broadenings arise due to a given dephasing parameter γ_{eg}, is very similar to the one used in the popular Nuclear Ensemble Approach (NEA), which is described in Section 3.2. By using eq. 13 we obtain the linear spectrum as a sum of Lorentzian contributions, which may be accurate enough in some cases but that does not suffice to appropriately account for complex absorption patterns as those featured in cross sections recorded at low temperatures where vibronic features are prominent.

[19.3.1.1 Spectral lineshapes in linear absorption]

Further detail can be included by accounting for spectral lineshapes as those coming from the DBO model outlined in Section 2.2 above. A brief scheme of the different contributions to the broadening is shown in Fig. 4: from a stick spectrum that requires just transition energies (or electronic energy differences) and associated transition dipole moments (ω_{eg}, μ_{eg}), to a (discrete) vibrationally resolved spectrum that includes contributions from normal modes and frequencies (ω_k). It can be further developed with the inclusion of the finite lifetime of the accessed state, which can be included through a lifetime constant τ_{ab}^{-1}

that can be obtained either theoretically or experimentally. Homogeneous broadenings can then be considered through nuclear relaxation (either by projecting the normal mode displacements or fitting them to an MD simulation) and static disorder (σ_a) effects, and inhomogeneous broadening can be included through the dynamic disorder (i.e. by Fourier-transforming $C_{aa}(t)$) which is obtained by considering multiple solvent rearrangements around the solute.

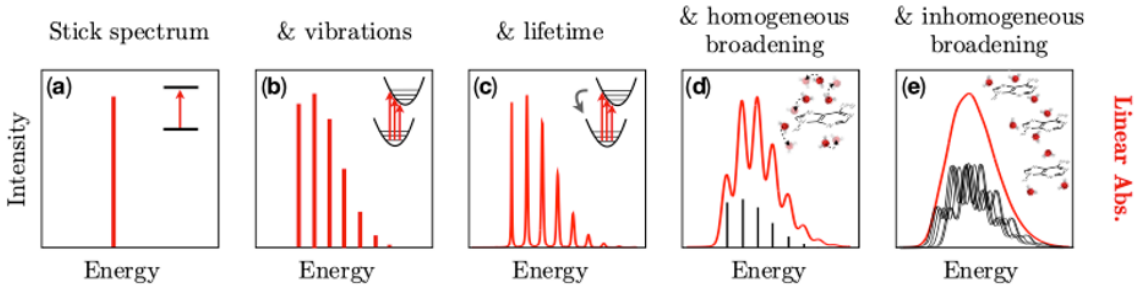

Figure 4. Schematic representation of the different contributions to the spectral lineshape: (a) stick spectrum, (b) stick spectrum plus vibrations, (c) addition of the lifetime broadening, (d) inclusion of homogeneous broadening and (e) inhomogeneous broadening. The insets of each panel depict the physical origin of the different contributions. Adapted from Ref. 37 with permission from the Royal Society of Chemistry.

A couple examples have been selected to showcase the application of the DBO model in simulating linear absorption and its accuracy.

The first is azobenzene, a molecule of great interest due to its ability as a molecular photoswitch, and already proposed in chapter 7 as case study for polaritonic chemistry issues:[61] it possesses a *trans* and a *cis* conformation that can be interconverted upon external radiation thanks to their well-separated absorption maxima. The *trans* conformation is more stable and the one measured in linear absorption experiments, the *cis* conformation being accessible in time-resolved measurements. To model azobenzene, we develop eq. 12 by resolving the dephasing γ_{eg}

$$R^{(1)}(t_1) = \left(\frac{i}{\hbar}\right)\Theta(t_1)\sum_e \left|\mu_{eg}\right|^2 e^{-i(\omega_{eg}-i\tau_{ge}^{-1})-2g_{ee}(t_1)} \qquad (14)$$

into contributions from the lifetime (τ_{ge}^{-1}) and the lineshape function $g_{ee}(t_1)$, which is the $g_{ab}(t_1)$ lineshape function referred in this case to the populated state e. A step-by-step derivation of this equation can be found elsewhere.[22,23] τ_{ge}^{-1} is the overall lifetime constant fitted by a pump-probe experiment and its numerical value is in this case extracted from the literature,[49] even if it could also be obtained directly from theoretical estimates.[62] In the absence of solvent interactions, the lineshape function $g_{ee}(t_1)$ can be computed using an expression of the spectral density $J_{ab}(\omega)$ which expands the ground state normal modes to provide an estimate of the homogeneous broadening

$$J_{ab}(\omega) = \pi \sum_k \tilde{d}_{ak}\tilde{d}_{bk}\omega_k^3[\delta(\omega - \omega_k)] \qquad (15)$$

Which is the spectral density used in eqs. 5 and 9 giving rise to $g_{ab}(t_1)$. In linear absorption only autocorrelation terms are required (i.e., $a = b$), and δ is an arbitrary broadening which is set to 5 cm^{-1}. The Condon approximation is used here for the transition dipole moment μ_{ab}, which implies considering it to be independent of the geometry and then taken as equal to its value at the ground state (GS) minimum throughout the multiple distortions exerted by projecting the geometry along the different active normal modes.

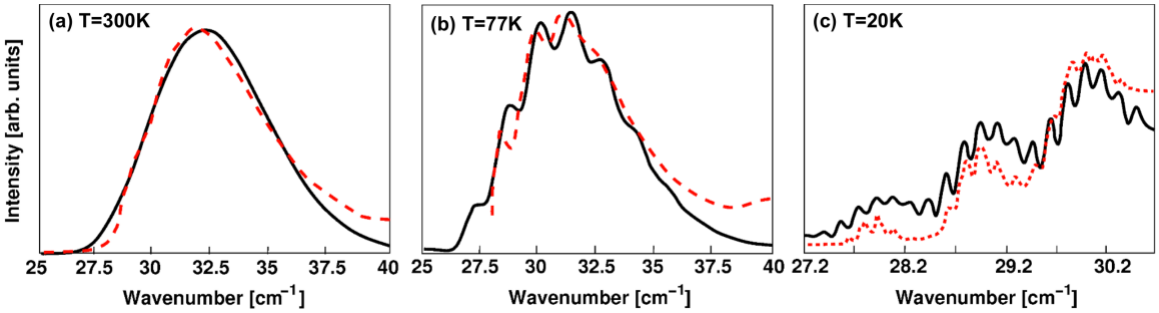

Figure 5. Experimental (red dashed) and simulated linear absorption spectra for trans-azobenzene obtained at room temperature (a), 77K (b) and 20K (c). The room temperature spectrum was measured in Ref. 49, the 77K spectrum was taken from Ref. 63 and the 20K spectrum (in a dibenzyl crystal) was taken from Ref. 64. Reproduced from Ref. 49 with permission from the American Chemical Society.

Substituting the different parameters on eq. 14 yields the spectra shown in Fig. 5, where theory is depicted in thick black and experiment in dashed red lines. Upon simple inspection it is worth noting the remarkable agreement across the different temperatures measured: at room temperature (a), enough thermal energy is available to produce a significant homogeneous broadening expected in such a flexible molecule like azobenzene which covers any vibronic features, while at 77K (b) and 20K (c) the emergence of

vibrational progressions can be easily noticed. The model, based on the lineshape functions $g_{aa}(t_1)$ is therefore able to reproduce not only peak positions and relative intensity, but also vibrational progressions and how these emerge at low temperatures. This can be understood by noting the $k_B T$ term in the denominator in eq. 8.

The different spectra therefore qualitatively capture the complex spectral lineshapes measured experimentally but are still unable to fully capture experiment: this is due to the fact the DBO model relies on a bath of uncoupled harmonic oscillators (as described in Section 2.2), which makes lineshapes overly harmonic with respect to experiment (see Fig. 5b and 5c) and that highlights the inherent anharmonicity of flexible molecular systems. Despite this, the overall agreement between theory and experiment is remarkable, and the DBO model albeit computationally complex and expensive allows connecting experiment and theory from first principles.

The second case we will analyse is pyrene. Pyrene is a polycyclic aromatic hydrocarbon characterised by an excited state lifetime in the picosecond regime, a high fluorescence quantum yield, an UV absorption spectrum displaying a clear vibronic progression, an ultrafast internal conversion to the S_1 state, and a few characteristic Excited State Absorption (ESA) signals. All these photophysical properties, together with its photostability, have made of pyrene a suitable probe of both experimental and theoretical spectroscopy techniques. An additional advantage of pyrene from a theoretical point of view is its molecular rigidity, which justifies the use of harmonic models like the DBO.

The linear absorption spectrum between 28-33000 cm^{-1} (region in which the only bright state is the S_2 H→L L_a state) was computed as the Fourier transformation of the first-order response function $R^{(1)}(t)$.[48] The latter was formulated in the SOS framework (i.e. expanding it in the basis of the system eigenstates) adopting two main approximations. First, electronic inter-state interactions were neglected, which means that the system is considered to evolve on a single adiabatic surface and no population transfer from one state to another is allowed. This, together with the Condon approximation for the transition dipole moment μ_{eg} (i.e. considered to be independent of the geometry and then taken as equal to its value at the GS minimum), determines that the general expression of the first-order response function, eq. 12, is expanded as follows

$$R^{(1)}(t) = i\left|\mu_{eg}\right|^2 e^{-i\int^t \left(E_e(\tau)-E_g(\tau)\right)d\tau} = i\left|\mu_{eg}\right|^2 \sigma_{eg}(t) \qquad (16)$$

where $\sigma_{eg}(t)$ is the coherence dynamics between states g and e, being in this case the GS and L_a states, respectively.

Second, the uncoupled DBO model was adopted for the GS and L_a Potential Energy Hypersurfaces (PEHs): i.e. both PEHs are considered to be the same quadratic function of the coordinates, being consequently described by the same normal modes k and corresponding frequencies ω_k, but having different equilibrium positions (see Section 2.2). $\sigma_{eg}(t)$ can then be written as

$$\sigma_{eg}(t) = e^{-i\int^t \left(E_e(\tau)-E_g(\tau)\right)d\tau} = e^{-i\omega_{eg}t+g(t)} \qquad (17)$$

where ω_{eg} is the adiabatic transition energy between the states g and e and $g(t)$ is the lineshape function, that for the DBO model is equal to:

$$g(t) = -i\sum_k D_k \int^t e^{-i\omega_k\tau}d\tau \qquad (18)$$

where ω_k and D_k are the frequencies and amplitudes of the active normal modes.

These parameters were extracted in this case from a 250 fs adiabatic semi-classical CASSCF(2,2)/6-31G* 0K-trajectory (i.e., starting the excited state dynamics from the FC region without kinetic energy) on the bright L_a state: ω_{eg} was obtained as the energy gap between the GS in its minimum and the first encountered relative minima of L_a along the dynamics, while ω_k and D_k were obtained fitting the $E_{La}(t) - E_{GS}(t)$ energy difference along the dynamics with a Fourier series. The expression for $R^{(1)}(t)$ then becomes

$$R^{(1)}(t) = i\left|\mu_{eg}\right|^2 e^{-i\omega_{eg}t+g(t)-\Gamma t} \qquad (19)$$

with an added phenomenological rate

$$\Gamma = \gamma + \frac{1}{T_e} \qquad (20)$$

where T_e accounts for the lifetime of the L_a state. This corrects the infinite lifetime given to the L_a state as a result of neglecting electronic inter-state interactions, and adds a term γ (set to 200 cm^{-1}) to account for homogeneous broadening due to the dynamic interactions with the solvent.

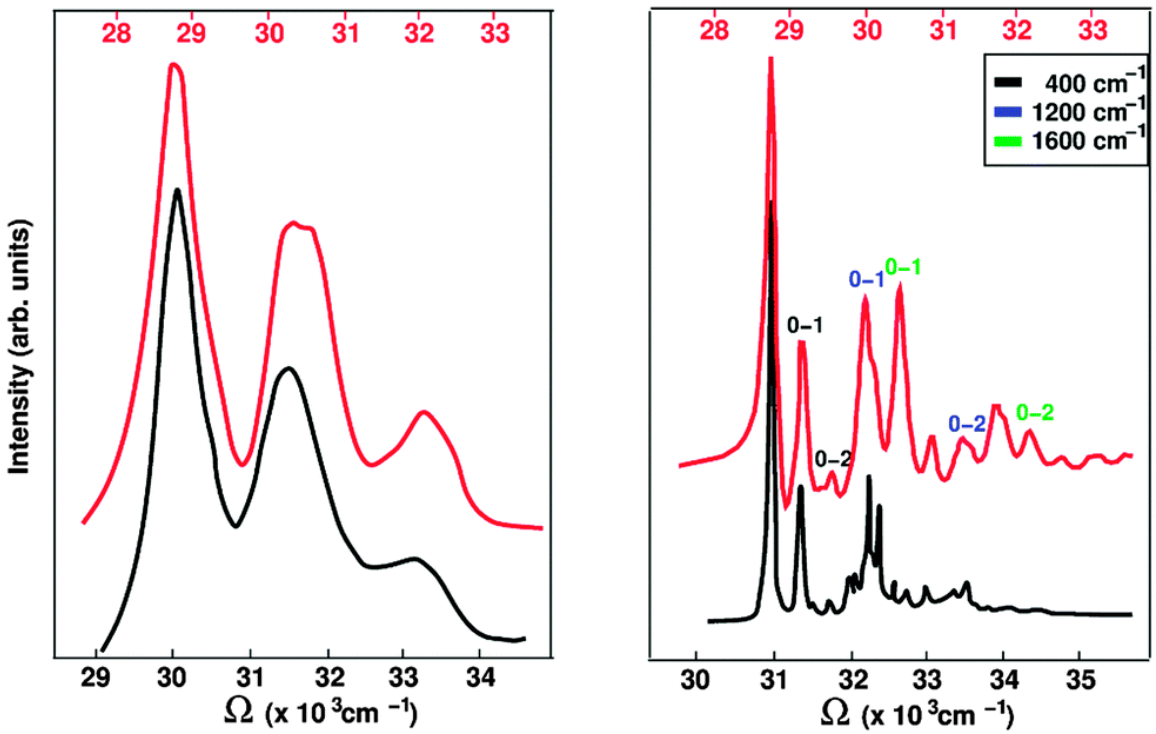

Figure 6. Experimental (black line) and theoretical (red line) linear absorption spectrum of pyrene recorded in aqueous solution at room temperature (left)[65] and in a Ne-matrix at 6 K (right).[66] Theoretical and experimental spectra are normalised with respect to the fundamental (0–0) transition. Spectral bandwidth was modelled with a lifetime broadening parameter of 125 cm^{-1} (corresponding to the 85-fs lifetime of the L_a state). A dephasing rate constant of 200 cm^{-1} was used in the aqueous spectrum to include fluctuations due to solute–solvent interactions. The overtones of the three dominant modes which contribute to the vibrational progression are labelled. Reproduced from Ref. 48, with permission from the Royal Society of Chemistry.

The absorption spectrum of pyrene is shown in Fig. 6 at (a) room temperature and (b) Ne-matrix at 6K, where black lines denote experiment and red stands for the theoretical model proposed above. The 6K simulation was carried out by neglecting any broadenings due to dephasing (i.e. $\gamma = 0$). The remarkable agreement between the theoretical and experimental spectra validates the approach used, and in particular its ability to reproduce the vibronic progression observed experimentally, composed in the room temperature spectrum of three bands separated by around 1400 cm^{-1}, in which the 0-0 transition is the most intense. Three main vibrational modes at 400, 1200, and 1600 cm^{-1} resulted to dominate the initial relaxation dynamics of pyrene after population of the L_a state.

The last example examined is adenine, also known as 6-aminopurine, one of the nucleobases featured in our DNA. Excited state properties of DNA are of interest as they relate to healthcare concerns like skin cancer melanoma, which makes it a molecular system of broad interest to the scientific community. Adenine possesses a limited range of

electronic excited states accessible via absorption, mainly being the ππ* L_a and L_b states,[67,68] the former being the bright and absorbing state.

In this case all lineshape contributions (both homogeneous and inhomogeneous broadenings) as shown in Fig. 4 are included in the simulation. To do this, the spectral density is split on two separate contributions[36–38]

$$J(\omega) = J^H(\omega) + J^L(\omega) \qquad (21)$$

where $J^H(\omega)$ stands for contributions arising from the high-frequency sector of the spectrum and are simulated using uncoupled normal mode displacements as it has been done above for azobenzene[49] following eq. 15. $J^L(\omega)$, on the other hand, accounts for the low-frequency sector that is included through the fluctuations recorded in the autocorrelation function and that represent weak solvent-solute (water-adenine) interactions. These interactions are included following the procedure described in Section 2.3 and use an MD simulation to obtain a sequence of time-dependent water rearrangements over time while the adenine moiety is frozen, as to not double-count contributions due to homogeneous broadening that are already included in $J^H(\omega)$.

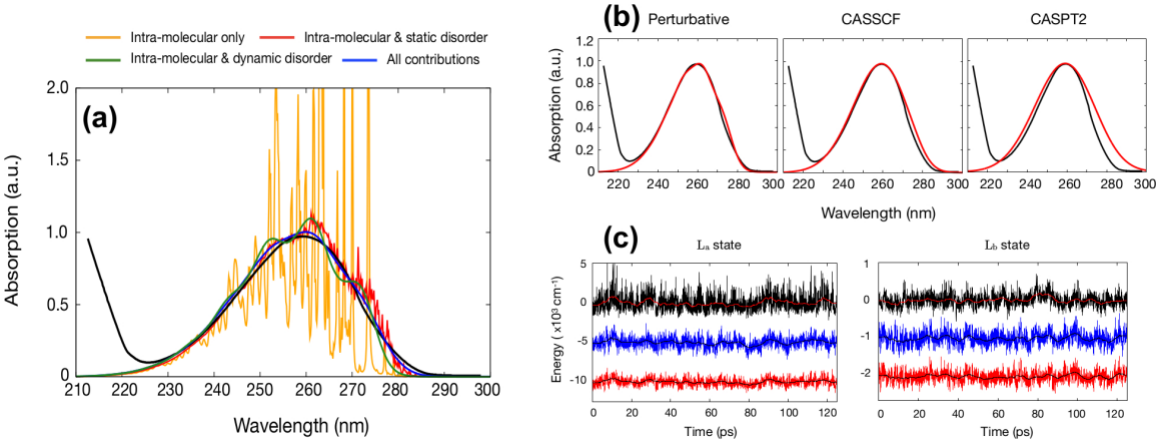

Figure 7. (a) Simulation of the linear absorption spectrum using the perturbative model using only selected disorder contributions: static + dynamic disorder (i.e. all; in blue), only dynamic disorder (green), only static disorder (red) and no disorder (i.e. only intramolecular contributions; orange). (b) Comparison between the different simulated linear spectra of adenine in water: Perturbative, CASSCF and CASPT2. The L_a state transition is centred on the experimental maximum to facilitate comparison, which implies a 2600, 1200 and 1100 cm^{-1} shift, respectively. No lifetime broadening is

included as it was shown to produce negligible changes to the lineshape. (c) L_a (left) and L_b (right) state energy flow along the MD trajectory. From bottom to top, these correspond to: Perturbative (red curve), CASSCF (blue curve) and CASPT2 (black curve). The experimental spectrum is shown in panels (a) and (b) and is taken from Ref. 69. Adapted from Ref. 37, with permission from the Royal Society of Chemistry.

An appealing aspect of this approach is that the spectrum can be deconstructed in each and every one its different broadening contributions: Fig. 7a shows the linear absorption spectrum of adenine and a systematic inclusion of the spectral lineshape, which allows observing how the different terms contribute towards the total broadening. As can be seen, intramolecular contributions are by far the largest in a flexible molecule that features ultrafast decays to the ground state as is adenine.[70] Static and dynamic disorder further modulates the broadening, particularly in the ~270 nm region which contributes to the asymmetry of the band. All contributions help balance the broadening to produce the blue curve that matches the experimentally obtained cross section,[69] which is reported in black.

Three different electronic structure theory methods were employed to produce the spectra (Fig. 7b) by computing the energy gap fluctuation functions: CASSCF, CASPT2 and a perturbative approach based on the CASSCF electron densities of the different states.[37] As can be seen, the CASSCF and perturbative methods yield a much better agreement with experiment than CASPT2. This is counterintuitive, as CASPT2 is known to retain more electron correlation and lead to more accurate vertical excitation energies. In this particular case, however, broadenings arise due to the fluctuations in the energy gap rather than how precise those are, and the single-state CASPT2 method can have some problems when dealing with multiple charged environments[71] leading to large energy deviations. This overestimates the broadening at the CASPT2 level, which appears as a Gaussian and is unable to describe the asymmetry of the band. The reason for this is given in Fig. 7c, where the different energy gap fluctuations for the bright L_a (left) and L_b (right) states are given: the black curves denote the CASPT2 method and feature multiple outliers, which vastly overestimate fluctuations and lead to an exaggerated broadening.

This shows the quality of the method used for obtaining the essential transition energies and transition dipole moments is important,[67,72–74] but so is how consistent the method is at describing $C_{aa}(t)$,[36–38] which contains the main information for describing the system's response and enters eq. 5 yielding the spectral density $J_{aa}(\omega)$.

[19.3.2 The Nuclear Ensemble Approach]

An alternative method that is simpler and possibly the most popular approach in the literature to obtain linear absorption spectral broadenings is the Nuclear Ensemble Approach (NEA) developed by Crespo-Otero and Barbatti.[75] This computational strategy

is based on the generation of a representative set of nuclear geometries and the subsequent simulation of the spectrum by calculating the vertical excitation energies and oscillator strengths.[56] The phenomenological broadening is added to the transitions by assigning a Gaussian or Lorentzian line shape to each one of them, which is centred at ΔE, with an associated δ that represents the Full Width at Half Maximum (FWHM) and with an area proportional to f. Some of the challenges of the NEA approach are the reliance on an arbitrary value δ and the reported difficulties to appropriately modelling vibrational broadenings. This computational strategy uses a semiclassical description of the light/matter interaction (the electromagnetic fields are treated as classical quantities and the matter is described by quantum mechanics) and the expression for the absorption cross section for a single transition is given by

$$\sigma_{abs,n}(E) = \frac{\pi e^2 \hbar}{2mc\epsilon_0 n_r E} \frac{1}{N_g} \sum_{j=1}^{N_g} \Delta E_n(\boldsymbol{R_j}) f_n(\boldsymbol{R_j}) g(E - \Delta E_n(\boldsymbol{R_j}), \delta_n) \qquad (22)$$

with e and m as the charge and mass of the electron, c is the speed of light in the vacuum, $\hbar$ is the reduced Planck constant, ϵ_0 is the vacuum permittivity, n_r is the refractive index at the spectral region of transitions, and N_g is the number of geometries sampled. For each one of the geometries in the nuclear ensemble it is necessary to know the nuclear coordinates given by $\boldsymbol{R_j}$ and both oscillator strength (f_n) and vertical transition energies (ΔE_n) from the ground state to the n^{th} excited state. $g(E - \Delta E_n(\boldsymbol{R_j}), \delta_n)$ provides the transition lineshape that is given by a normalised Gaussian

$$g(E - \Delta E_n(\boldsymbol{R_j}), \delta_n) = \sqrt{\frac{2}{\pi}} \frac{1}{\delta_n} \exp\left(\frac{-2(E - \Delta E_n)^2}{{\delta_n}^2}\right) \qquad (23)$$

where δ_n is the FWHM of the Gaussian that is usually determined phenomenologically, i.e., by testing different values and using the one that has the closest resemblance with the experiment. To obtain the complete cross-section of the NEA spectrum, all contributions of all possible excited states can be added, yielding

$$\sigma_{abs}(E) = \sum_{n=1}^{N_s} \sigma_{abs,n}(E) \qquad (24)$$

which is the total cross section accounting for all states included in the simulation. This work has been expanded on several fronts: Barbatti and co-workers extended it to enable the simulation of photoelectron spectral broadenings,[76] Isborn and co-workers combined the ideas of the NEA approach with a 2-level model system based on the generalised Brownian oscillator model within the CGF approximation truncated to second[36,77] and even third-order,[52] and both Dral and Isborn and co-workers have exploited machine learning tools to expedite the costly evaluation of the quantum mechanical quantities ($\Delta E, f$) that are the main bottleneck in these simulations.[57,78]

[19.3.2.1 Automated NEA broadenings with machine learning]

Recent work by Cerdán and Roca-Sanjuán[79] proposes a new computational strategy based on the NEA approach, where they use a probabilistic machine learning algorithm named Gaussian Mixture Models (GMMs) to avoid the phenomenological broadening assumption and the use of a subjective selection of the full-width, δ_n (a general introduction to machine learning algorithms, especially for photophysics, can be found in chapter 6).

In GMM-NEA a Monte Carlo (MC) method is applied to provide a statistical error. This error is inferred by a bootstrap re-sampling procedure as normality is not granted on ΔE and f. The procedure is based on the idea that it is possible to estimate statistics on a sample or population by sampling a dataset with replacements. Given a large dataset, we can take a small part of size N and estimate the statistical intervals desired. To increase the variability, a new dataset is taken from the original that is also of size N in which we have included new data (sample with replacement). In this case, a large number of new conditions are generated by randomly sampling replacements of N_g geometries and their ΔE_n and f_n from the original and available ones. For each one of these bootstrap replicas a NEA spectrum is computed ($\sigma_{abs,n}(E)$), obtaining for each wavelength a distribution of cross sections. By assuming a percentile bootstrap one can obtain lower and upper confidence intervals.

After the transformation of the conventional equation for the reconstruction of NEA spectra they obtain the following expression in terms of GMM parameters

$$\sigma_{abs,n}(E) = \frac{\pi E}{3\hbar c \epsilon_0 n_r} \sum_{k=1}^{K_n} \pi_{n,k} (\tilde{\mu}_{n,k}^2 + \tilde{\sigma}_{n,k}^2) \phi(E; \mu_{1,n,k}, \sigma_{1,n,k}^2) \qquad (25)$$

which is a continuous version of the NEA spectra that no longer depends on empirical bandwidths. In this expression $\tilde{\mu}_{n,k}$, the estimated mean, and $\sigma_{1,n,k}^2$, the variances, are given by

$$\tilde{\mu}_{n,k} = \tilde{\mu}_{2,n,k} + \rho_{n,k} \frac{\sigma_{2,n,k}}{\sigma_{1,n,k}} \left(E - \tilde{\mu}_{1,n,k}\right) \qquad (26)$$

$$\sigma_{1,n,k}^2 = \left(1 - \rho_{n,k}^2\right) \sigma_{2,n,k}^2 \qquad (27)$$

where $\rho_{n,k}$ is the correlation coefficient, n is the nth transition and k is the kth mixture of normal distributions in which the multivariate probability density function (PDF) has been decomposed. Subindices 1 and 2 make reference to the variables ΔE_n and $M_n \propto f_n$, respectively.

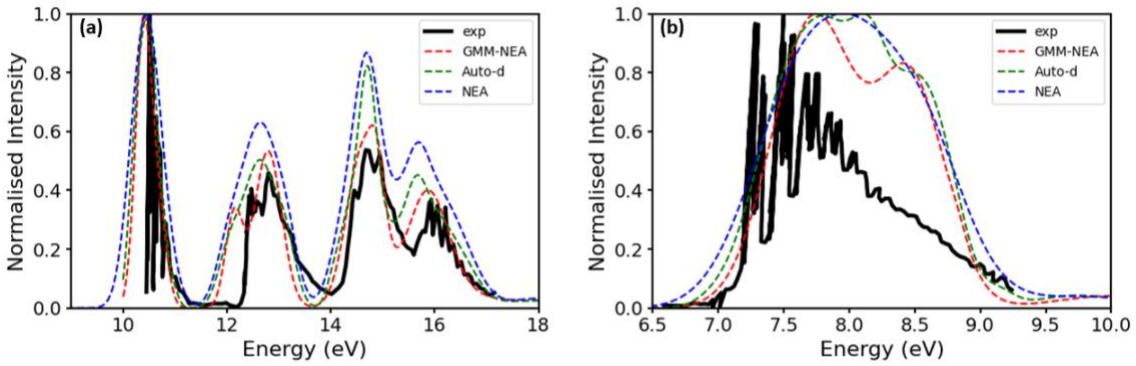

Figure 8. Comparison of theoretical photoelectron and linear absorption spectra of ethylene molecule obtained with different methods (blue for NEA, green for auto-δ and red for GMM-NEA) and the experimental photoelectron[80] and linear absorption[81] spectra registered in the gas phase. For the NEA spectrum $\delta = 0.3$ eV was selected.

Figure 8 shows the photoelectron (a) and linear absorption (b) spectra of gas phase ethylene using NEA ($\delta = 0.3$ eV), auto-δ (another method to automatically determine δ with machine learning tools)[79] and GMM-NEA, and compared with experiment. For all methods, a total of 50 geometries were used and for each geometry a total of 10 states were calculated, obtaining ten pairs of data points (ΔE_n and f_n, and Dyson norms[82,83] for photoelectron) characterising each of the electronic transitions. As can be seen, in both cases the most reliable simulation is provided by GMM-NEA, closely followed by auto-δ, which are able to predict both position and intensity as well as the relative width of the experimentally recorded signals. Despite being better than NEA in reproducing the experimental results, neither is able to capture the vibrational progressions observed experimentally: cross sections within NEA are obtained by convolving Gaussian/Lorentzian functions on multiple sampled points using only the energy gaps and oscillator strengths of the electronic transitions. The shortcomings in the description of vibronic features comes mostly from the need to sample vast amounts of points to recover such small features, which makes this approach perhaps not ideal for describing complex lineshapes. Our simulations also show GMM-NEA and auto-δ to accurately represent photoelectrons spectra (see Fig. 8a) based on intensities arising solely from Dyson norms,[76,82,83] which goes beyond what was tested in the original implementation[79] extending its applicability.

The conclusions obtained from our simulation on ethylene linear absorption and photoelectron spectra shown here are in line with those recently reported by Isborn and co-workers, which show how a NEA-like approach is insufficient to account for vibronic lineshapes:[84] when a correct representation of complex spectral broadenings is important, more sophisticated approaches to represent spectral lineshapes like those outlined above in section 3.1.1 should be used instead.

[19.4 Non-linear Spectroscopy]

To study temporally-resolved excited state processes, non-linear techniques are required. These use combinations of laser pulses which grant access to signals different from those described above in linear/steady-state absorption: Ground State Bleaching (GSB), Stimulated Emission (SE) and Excited State Absorption (ESA).

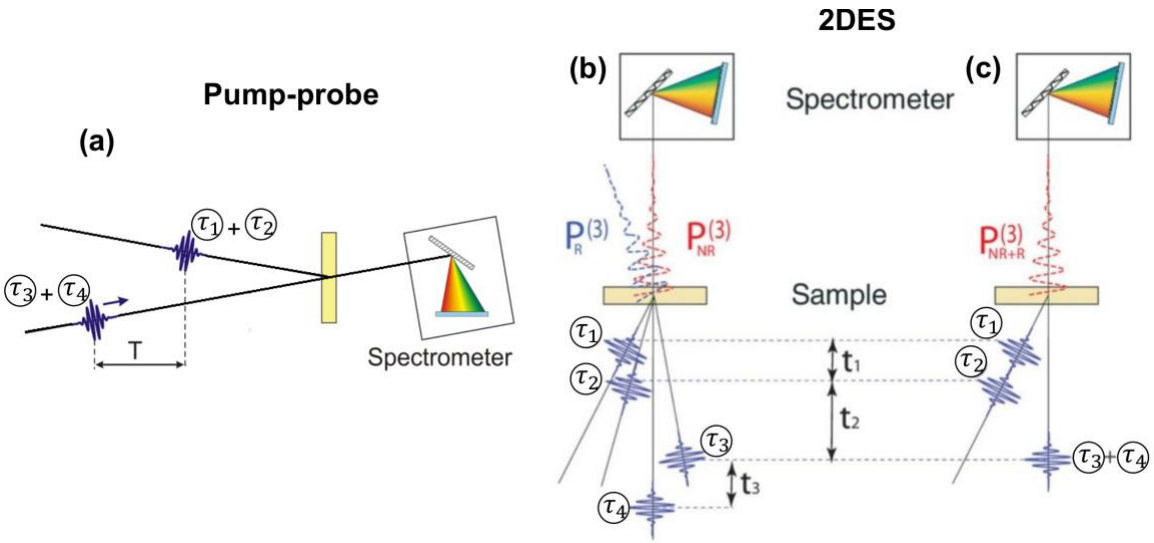

Figure 9. Scheme of the different non-linear spectroscopic techniques discussed in this chapter: (a) pump-probe, and (b) and (c) 2DES. Different experimental set-ups to measure 2DES are depicted: (b) photon echo non-collinear scheme (four-wave mixing), and (c) partly non-collinear pump-probe geometry. Rephasing ($P_R^{(3)}$, i.e. K_I), non-rephasing ($P_{NR}^{(3)}$,i.e. K_{II}) and quasi-absorptive ($P_{NR+R}^{(3)}$, i.e. K_I+K_{II}) polarisations are shown with their different directionality. Laser pulses are denoted by τ_i, and their numbering being related to the incidence order, and t_i referring to the time intervals between laser pulses. Adapted from Ref. 85 with permission from Springer.

Non-linear spectroscopies monitor excited state dynamics by measuring (or probing) the sample at different delay times (T, see Fig. 9a) spaced between the incident laser pulses: several set-ups are available but we will focus on ways to simulate pump-probe and 2DES experiments, which are the most frequently reported in the literature.

Both pump-probe and 2DES are 3rd order non-linear optical spectroscopies, and they feature similarities in their set-ups. Fig. 9 shows a scheme of a pump-probe experiment (a), and the two most common set-ups for 2DES (b and c). Compared to the linear absorption experiment shown in Section 3, non-linear set-ups are significantly more complex: by

featuring 4 separate light-matter interactions, different phase-matching conditions are also possible, which lead to different polarisations being measured.

Amongst 3rd order non-linear optical spectroscopies, 2DES provides enhanced spectral and temporal resolution thanks to the use of ultrashort broadband laser sources.[14–16,22,23,86,87] Its development in the late 90s ports many of the advances made in 2D Nuclear Magnetic Resonance (NMR) techniques a decade earlier to the optical domain,[86] enabling the study of multichromophoric (particularly those strongly interacting) with its enhanced dimensionality.[6] At a difference from standard pump-probe techniques, 2DES can separate line broadenings in their inhomogeneous and homogeneous origin,[85] and it registers microscopic couplings between different chromophores through the presence of cross peaks and their oscillations, which are often referred to as *quantum beats or beatings*.[88,89]

This type of experiment is more sophisticated, requiring 3 to 4 broadband (fs) ultrafast laser pulses used in sequence; a schematic example is given in Fig. 9b/c. This experiment produces a series of signals measured in terms of the 3rd order nonlinear polarisation of the resulting outgoing field after passing through the sample in phase-matched directions. The pulse sequence can moreover be aligned along different directions yielding distinct polarisation patterns, which can be tuned to reveal signals otherwise hidden and that further adds to its versatility.[23,90] Experimentally, the most popular set-ups are the heterodyne-detected three-pulse photon echo (Fig. 9b) and the partially collinear "pump-probe" geometry (Fig. 9c); the former can fully resolve the 3rd order nonlinear response in terms of its rephasing (K_I=$-\tau_1 + \tau_2 + \tau_3$) and non-rephasing ($K_{II}$=$+\tau_1 - \tau_2 + \tau_3$) contributions, while the latter provide the combined "quasi-absorptive" (K_I+K_{II}) signal. Further details on the different set-ups and their pro/cons are beyond the scope of this chapter and can be consulted elsewhere.[17,18,85] From here onwards we will only refer to quasi-absorptive measurements, which means accounting for all different signals registered for K_I+K_{II} phase-matching conditions.

2DES mirrors the pulse sequence used in two-dimensional infrared (2DIR) techniques, where the time delay between the first two pulses (t_1) is called the coherence time, the delay between the second and the third (t_2) is the population time and the time after the third pulse corresponds to the detection time (t_3). This sequential light-matter interaction generates a third-order nonlinear response function which depends on all three pulses $S(t_1, t_2, t_3)$, from which 2D slices or maps are extracted by Fourier-transforming along times t_1 and t_3, producing spectra that depend on both excitation (Ω_1) and probe/detection (Ω_3) wavelengths leading to signals $S(\Omega_1, t_2, \Omega_3)$. By repeating this Fourier transformation at different population times (t_2) one can obtain a sequence of 2D maps that are equivalent to the time-resolved signals previously discussed for standard pump-probe spectroscopies, but which allow monitoring signal evolutions and their broadenings across both excitation (Ω_1) and detection (Ω_3) wavelengths. This technique therefore offers an advantage over standard pump-probe set-ups: it can resolve broadenings along the excitation wavelength, which measures the couplings between different chromophores upon excitation as well as any potential energy transfer or interaction across moieties.[88]

Time-resolved photoelectron spectroscopy experiments represent another popular venue for probing excited state processes and that can be used in non-linear set-ups similar to pump-probe spectroscopy. Plenty of developments have been reported elsewhere for simulating these types of signals,[76,91–97] which we have left out of this chapter for the sake of simplicity.

[19.4.1 Non-linear spectroscopy in the Liouville space]

In non-linear spectroscopies we are interested in the 3rd order induced polarisation, which is the signal registered in pump-probe and 2DES set-ups. As noted in Section 2.1, the density matrix can be evolved in time using the Liouville-von Neumann equation, and the external optical fields can be included (assuming they are weak) as a perturbation.[19,22,23] Rearranging the density matrix in terms of time intervals t_i between pulses (τ_i), we can write the third-order expression as

$$\begin{aligned} P^{(3)}(t) &= Tr\left[\hat{\mu}\hat{\rho}^{(3)}(t)\right] \\ &= \int_0^\infty dt_3 \int_0^\infty dt_2 \int_0^\infty dt_1 \, R^{(3)}(t_3, t_2, t_1) \\ &\times E(t - t_3)E(t - t_3 - t_2)E(t - t_3 - t_2 - t_1) \end{aligned} \qquad (28)$$

where $t_1 = \tau_2 - \tau_1$, $t_2 = \tau_3 - \tau_2$ and $t_3 = \tau_4 - \tau_3$ are time differences between pulses and τ_{1-4} denote the four laser pulses used in sequence and ordered in time (i.e. τ_1 comes before τ_2, etc…), τ_4 being the local oscillator that heterodynes the signal and carries it to the detector (see Fig. 9). $R^{(3)}(t_3, t_2, t_1)$ is the response function of the system exposed to the different light-matter interactions in terms of the laser pulses represented as electric fields $E(t)$. This expression can be simplified if we assume that pulse duration is short enough. This is referred to as the *impulsive limit*,[19,23] i.e. the limit in which pulse duration is less than a single vibrational oscillation period, and it allows us to move from the signal expressed in terms of the induced polarisation to the system's response, which can be more easily evaluated theoretically:

$$R^{(3)}(t_1, t_2, t_3) = \left(\frac{i}{\hbar}\right)^3 Tr\left[\hat{\mu}\mathbb{G}(t_3)\left[\hat{\mu}, \mathbb{G}(t_2)\left[\hat{\mu}, \mathbb{G}(t_1)[\hat{\mu}, \rho(0)]\right]\right]\right] \qquad (29)$$

As introduced in Section 3.1, $\mathbb{G}(t)$ is the retarded Green's function that includes phenomenologically population transfer (i.e. the time evolution of the density matrix after irradiation) within the impulsive limit.[22]

Imposing phase-matching conditions gives access to different Liouville pathways,[22,23] which are associated to different physical processes due to the distinct interactions with external fields (or lasers), and whose sum forms the full response of the system

$$R_{K_I}^{(3)}(t_1,t_2,t_3) = \sum_{i=GSB,SE,ESA} R_{K_I,i}^{(3)}(t_1,t_2,t_3) \qquad (30)$$

where sub-index i goes over the different mechanisms: excited state absorption (ESA), stimulated emission (SE) and ground state bleaching (GSB).

The different Liouville pathways and the mechanisms available can be conveniently expressed in terms of double-sided Feynman interaction diagrams: Fig. 10 shows the ESA diagram for the rephasing (K_I) response, and a pulse-by-pulse sequence of events and how these build up to the mathematical expressions used below. The bottom panels represent the different elements of the density matrix operator $\hat{\rho}$ reached during the pulse sequence, and how these convert into the different formulas and lead to the different dependencies on transition energies ω_{ab} and transition dipole moments μ_{ab}. Notice the negative sign in the K_I rephasing condition for pulse τ_1, which leads to a positive exponential in the first term of the SOS expression in Fig. 10 and thus appears on the right-hand side of the double-sided Feynman diagram, whereas pulses τ_2 and τ_3 appear on the left-hand side of the diagram and lead to negative terms. τ_4 represents the local oscillator that heterodynes the signal and carries it to the detector.

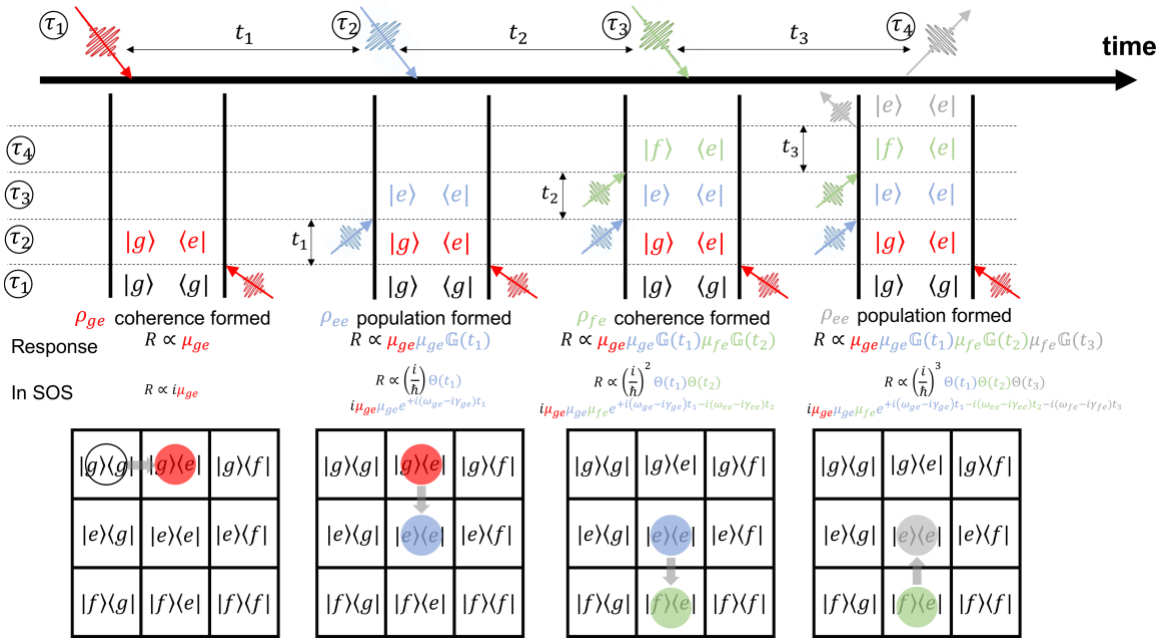

Figure 10. Pulse-by-pulse sequence of the double-sided Feynman diagram for ESA in the rephasing (K_I) phase-matching condition, together with the associated response function, its expansion into the eigenvalue representation within the SOS approach (equivalent to eq. 31 below) and a diagram to walk through the specific density matrix ($\hat{\rho}$) terms being

reached at each step (assuming we start from the equilibrium ground state density $\hat{\rho}_0$, shown as an empty black circle). All diagrams are based on a 3-state level model: g represents the electronic ground state, e the electronic excited states that may be populated within the pump (population) sequence ($\tau_1 + \tau_2$) and f refer to higher-lying electronic excited states that can be reached from e in ESA signals.

[19.4.2 Non-linear spectroscopies within a static approximation]

The crudest approximation to 2DES we introduce is to assume the system to be static, i.e., to switch off all dynamic evolution of the density matrix between τ_2 and τ_3 pulses (see Fig. 10) meaning we assume our signal to arise from a single geometry, which provides a sort of equivalent to a "steady-state" version of this complex spectroscopy.

Assuming this, we can develop eq. 29 analogously to how we did with eq. 12 in Section 3.1 for linear absorption, leading to

$$R_{ESA}^{(K_I)}(t_1, t_2, t_3) = \left(\frac{i}{\hbar}\right)^3 \Theta(t_1)\Theta(t_2)\Theta(t_3) \sum_{e,f} |\mu_{ge}|^2 |\mu_{ef}|^2 \times e^{+i(\omega_{ge} - i\gamma_{eg})t_1 - i(\omega_{ee} - i\gamma_{ee})t_2 - i(\omega_{ef} - i\gamma_{fe})t_3} \quad (31)$$

which upon Fourier transforming along t_1 and t_3 becomes[29]

$$P_{ESA}^{(K_I)}(\Omega_1, t_2, \Omega_3) = \sum_e \frac{|\mu_{ge}|^2}{\Omega_1 + \omega_{ge} - i\gamma_{eg}} \cdot \frac{|\mu_{ef}|^2}{\Omega_3 - \omega_{ef} + i\gamma_{fe}} \times e^{-i(\omega_{ee} - i\gamma_{ee})t_2} \quad (32)$$

where the last term $e^{-i(\omega_{ee} - i\gamma_{ee})t_2} = 1$ for those cases when $t_2 = 0$, leading to a set of points across Ω_1 and Ω_3 frequencies with broadenings proportional to their respective dephasings (γ_{eg} and γ_{fe}, considering a 3-state model as in Fig. 10). This particular equation refers to ESA within the K_I phase-matching condition, and analogous expressions can be obtained for the GSB and SE signals (as well as for ESA, GSB and SE within K_{II}) and are reported in detail elsewhere.[22,23,29]

This rather severe approximation has been used in a number of studies to assess the accuracy of the underlying electronic structure in describing the different signals appearing in the 2DES maps, and an example is provided in Fig. 11 for the specific case of adenine.

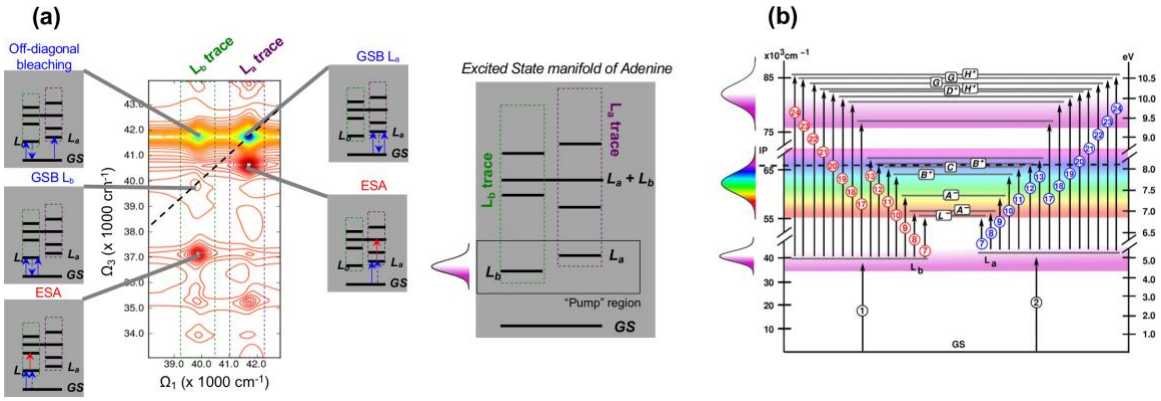

Figure 11. (a) 2DES spectrum of adenine within the static approximation at $t_2 = 0$ and considering broadenings purely due to a single and equal dephasing constant of $\gamma = 200$ cm^{-1} for all transitions considered. Arrow diagrams depicting the pulse sequence leading to each signal are also provided, blue representing the negative (SE, GSB, ODB) and red the positive (ESA) contributions, the diagonal being marked by a dashed black line. (b) Scheme describing the vast excited state manifold accessible to adenine from both ππ* L_a and L_b excited states. Adapted from Ref. 67 with permission from the American Institute of Physics.

Fig. 11a shows a simulated 2DES experiment for adenine, with transition diagrams depicting the specific light-matter interactions behind SE, GSB, Off-Diagonal Bleaching (ODB) and ESA signals. GSB signals appear along the diagonal (marked with a dashed black line), whereas SE, ESA and ODB signals appear along the traces of the respective states populated during the first sequence of two pulses (i.e., the "pumped" states), ππ* L_a and L_b. The trace of L_a (in purple) appears to be more intense, particularly its GSB, with respect to L_b, as this signal is commensurate with the oscillator strength for their linear absorption that shows L_a to absorb substantially more than L_b. Besides this, which is also observed in the ODB along the L_b trace (in green), an ESA signal with significant intensity appear along both L_a and L_b traces in different parts of the spectrum, corresponding to the ESA transitions to their respective doubly excited states. This simple model allows observing roughly where the main signals will emerge, and even to distinguish between the state responsible for which signals: this is useful for monitoring excited state processes and provides the extra value of recording signals coming from different states in distinct parts of the spectrum thanks to the additional Ω_1 dimension.[14–16,18,19,98,99]

This example showcases what can be achieved with the static approach, which is a simple approximation to understand roughly where the signals will be placed in a 2DES experiment. This approach has been used in several systems, including all other

nucleobases,[72,73] the adenine-adenine[68,100] and adenine-uracil[101] monophosphate dimers, as well as other biologically relevant molecules like benzophenone,[102] indole[103,104] and other aromatic amino acid-containing peptides,[90,105,106] and the protonated Schiff base 11 in Rhodopsin.[107–109]

The static approach does not necessarily mean that the spectra refers to $t_2 = 0$: kinetic models can be used to take into account the time evolution of the signals while still approximating the 2DES spectrum to arise from a single geometry (i.e., excited state minima, for example) with approximated broadenings.[101] On the other hand, molecular dynamics schemes can be used to obtain $t_2 = 0$ estimates while including lineshape contributions due to energy fluctuations, as is shown below in Fig. 13a for pyrene.

One additional aspect to highlight is the vast manifold of states accessible in these spectroscopies (Fig. 11b): GSB and SE signals require only a description of the electronic states that are directly populated (or "pumped") with the pump sequence (i.e. $\tau_1 + \tau_2$ in Fig. 9), but ESA signals reach higher-lying electronic states that can be challenging to describe.[37] These high-lying states often feature doubly excited character (i.e. their underlying wave function is described by a double electron promotion[110]) which is difficult to assess theoretically and that is beyond most methods based on a linear response approach like time-dependent density functional theory.[111] Moreover, energy gaps between electronic excited states reduce as we go higher in energy, meaning that there are a vast amount of states accessible and related to ESA signals: methods able to describe single and double excitations consistently throughout vast energy ranges are thus essential to describe ESA signals.

[19.4.2.1 The Nuclear Ensemble Approach to non-linear spectroscopy]

A NEA-like scheme can also be used to obtain estimates of non-linear spectroscopic signals based on potential energy surface characterisations. This implies characterising the electronic excited state minima where population is trapped along the excited state decay, and assuming these minima to feature a prominent and fixed single electronic state character from which signals might be computed. The rationale behind this is straightforward: minima act as population traps, and molecular systems are expected to spend significant amounts of time on these stationary points. Technically, all that is required is using eq. 22, as done within the NEA approach for linear absorption (without the pre-factor that converts into extinction coefficients), and looking instead at excited state absorptions (i.e. $S_1 \rightarrow S_n$, and their associated ΔE and f), averaging over each one of the available transitions and building a total signal that represents a crude approximation of the excited state absorption. Negative components due to GSB/SE can be added by considering the $S_1 \rightarrow S_0$ emitting features, put together forming an approximation of the overall pump-probe spectrum.

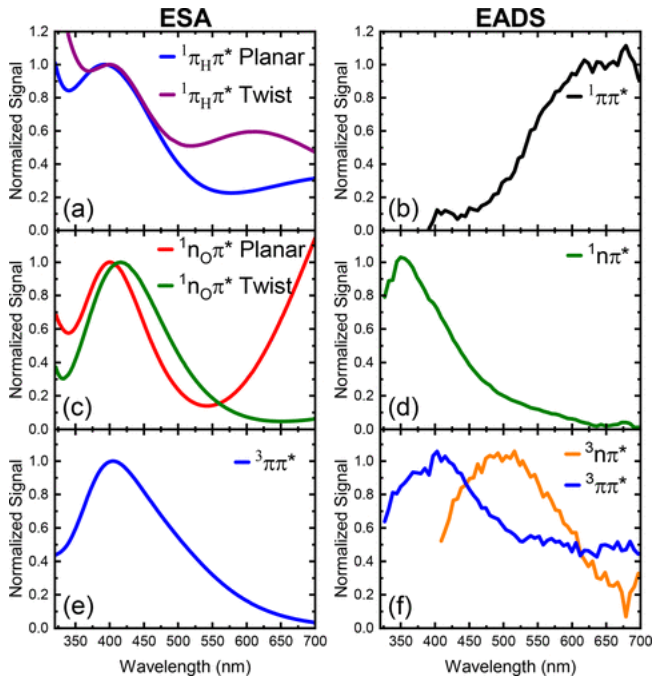

Figure 12. Panels (a), (c) and (e) show normalised excited state absorption features of water-solvated uridine computed within a CASPT2/MM approach.[112,113] Panels (b), (d) and (f) show normalised evolution associated difference spectra (EADS) of uridine monophosphate in PBS at pH 7.3, determined from a global fit analysis of the multidimensional transient data. Reproduced from Ref. 114 with permission from the American Chemical Society.

This approach has been thoroughly used in the literature,[74,115–119] particularly in the context of DNA excited state dynamics,[71,111–113] and has yielded surprisingly reasonable results. Fig. 12 shows the remarkable agreement found between the simulated ESA signals (arising from the optimised excited state minima) of water-solvated uridine and the experimentally recorded signals in uridine monophosphate. Qualitative agreements can be seen for the optically dark $^1n_O\pi^*$ state (panels (c) and (d) in Fig. 12), which facilitate assignment of this otherwise challenging signal, and that also enable the signal to state assignment of the triplet $^3\pi\pi^*$ state (panels (e) and (f)). It is important to note that this study was preceded and motivated by previous theoretical studies which predicted the ESA signals of pyrimidine nucleosides in solution just using the NEA approach;[112,113] this showcases how qualitative and valuable spectroscopic information can be obtained even when using rather simplified approaches.

[19.4.3 Spectral broadenings in non-linear spectroscopies]

Broadenings in non-linear spectroscopy adopt more complex expressions compared to its linear counterpart, as multiple Feynman diagrams enter the different parts of the response function depending on the phase-matching condition considered. This leads to multiple expressions (for each phase-matching condition and each diagram therein) which has to be

included towards the total signal, and where broadenings become multipoint lineshape functions, i.e. functions that depend on linear combinations of multiple lineshape functions ($g_{ab}(t)$ in Section 2.2) described above.

We start analysing broadenings in non-linear spectra by looking again at the pyrene example introduced in Section 3.1.1 for linear spectra. In this particular case, and assuming a single trajectory to sample the fluctuations of the excited states to be included in the description of the spectrum, the ESA signal can be formulated as:

$$R^{(3)}_{K_{I,ESA}}(t_1,t_2,t_3) = i\Theta(t_1)\Theta(t_2)\Theta(t_3)\sum_f \left|\mu_{fe}(\tau_3)\right|^2\left|\mu_{eg}\right|^2 e^{-i\omega_{eg}t_1+g(t_1)-\Gamma t_1}e^{-\frac{t_2}{T_e}}e^{-i\int^{t_3}\left(E_f(\tau)-E_e(\tau)\right)d\tau-\Gamma t_3} \quad (33)$$

where f indicates the manifold of excited states spectroscopically bright from the e (initially excited or "pumped") manifold. The equation is obtained assuming an adiabatic description (i.e., neglecting inter-state interactions and consequently population transfer) during both t_1 and t_3, which considers that along both times the system is evolving along the e manifold. Moreover, in eq. 33 the DBO model (see Section 2.2) is adopted along t_1, and the geometry dependency of the transition dipole moment included only along t_3.

Making the further approximation that the coherence dynamics is slower than the duration of the experiments (i.e., during t_1 and $t_3$the molecule does not have enough time to evolve) leads to the following simplification, equivalent to the static approach:

$$R^{(3)}_{K_{I,ESA}}(t_1,t_2,t_3) = i\Theta(t_1)\Theta(t_2)\Theta(t_3)\sum_f \left|\mu_{fe}\right|^2\left|\mu_{eg}\right|^2 e^{-i(E_e-E_g)t_1-\Gamma t_1}e^{-\frac{t_2}{T_e}}e^{-i(E_f-E_e)t_3-\Gamma t_3} \quad (34)$$

Such an approach considers that the system can be represented in a single geometry during both t_1 and t_3, and consequently $E_e - E_g$ and $E_f - E_e$ energy differences appearing in the expression have to be evaluated (i.e., analogous to ω_{ge} and ω_{ef}).

These equations were applied for the simulation of the quasi-absorptive 2D spectra for t_2 equal to 0 and 1 ps, taking into account the specific photophysics of pyrene: after excitation into the S_2 L_a state, the system undergoes an ultrafast internal conversion into the S_1 L_b state, in which remains trapped up to the picosecond time scale.

For t_2 equal 0 it is reasonable to consider that pyrene mainly evolves along the same state during the whole experiment, and consequently in the $R^{(3)}$ expression the e manifold includes only the initially excited L_a state along both t_1 and t_3. The f manifold was consequently taken as the bright states from L_a in the considered spectral window. Using a single-trajectory approach, the evolution along t_1 was described using the commented

DBO model, while the evolution along t_3 was taken into account evaluating the required $E_f - E_{La}$ and corresponding μ_{fLa} on 50 auxiliary points along the performed L_a dynamics, which were then fitted with a Fourier series. It is important to note that along the dynamics the energy gaps were obtained following the diabatic evolution of the states. Through the use of such Fourier series, a harmonic approximation was then intrinsically made also for describing the t_3 evolution. The $t_2 = 0$ 2D spectra was also computed with the static approach, in which case all required energies, $E_f - E_{La}$, and corresponding transition dipole moments were computed at the GS minimum. The comparison of the two approaches for the simulation of the $t_2 = 0$ 2D spectrum showed the importance of accounting for the evolution along t_1 and t_3 (see Fig. 13a). This is in agreement with the fact that along such times the system is evolving along L_a and far from a static equilibrium condition.

For $t_2 = 1\ ps$ it is important to account for the experimental evidence that pyrene remains trapped in the S_1 L_b minimum up to the picosecond time scale. This translates in the fact that the e manifold along t_3 is now formed by the L_b state, and that a static approach (along t_3) constitutes a very reasonable approximation. The f manifold was then formed by the bright states from L_b minimum in the considered spectral window. Comparison between experimental and theoretical spectra, shown in Fig. 13b, indeed validates the adopted simulation protocol: DBO single-trajectory approach along t_1 and static approach along t_3.

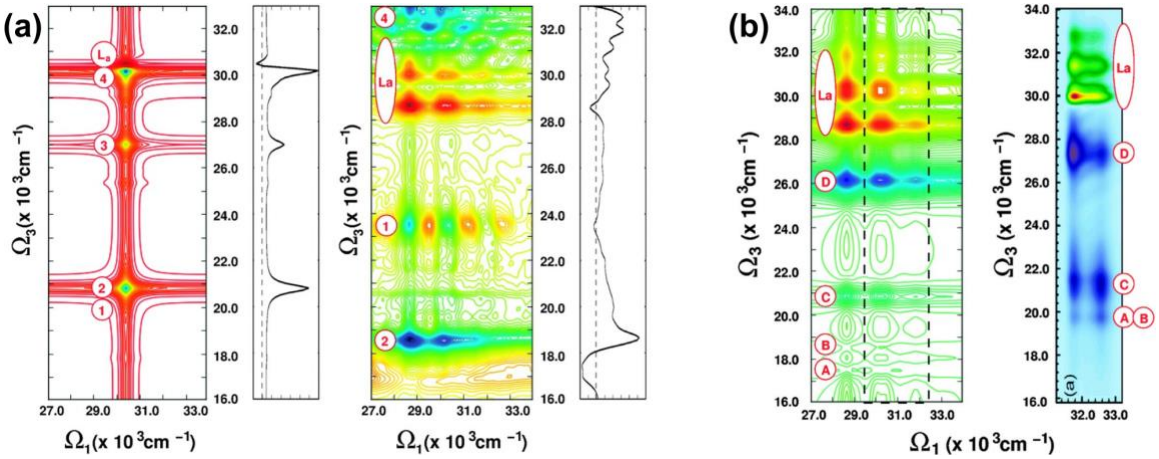

Figure 13. (a) Single geometry (left) vs dynamic (right) picture of the simulated 2DES quasi-absorptive spectrum of pyrene for $t_2 = 0$ ps.[48] (b) Theoretical[48] (left) and experimental[120] (right) quasi-absorptive 2DES of pyrene for $t_2 = 1$ ps. In the simulation it is assumed that probing occurs from the minimum in the dark S_1 L_b state, which is populated with a time constant of 85 fs and where the system is trapped on a timescale longer than the experiment. Reproduced from Ref. 48 with permission from the Royal Society of Chemistry.

As can be seen in Fig. 13, even when including as many approximations as those introduced in above, theory[48] is able to match the vibrational progressions observed experimentally.[120] Moreover, theory allows looking at much wider spectral windows, uncovering extra peaks on the left-hand side of the measured experiment; these are the main peaks along the

vibrational progression, and help assign the overtones recorded in the 2DES experiment. Another important aspect to highlight is how the lineshape remarkably resembles those of the experiment: this is in part due to pyrene being a very rigid and therefore harmonic system, which fits well with the approximations introduced within the DBO model. By having theory and experiment side-by-side a signal-to-state assignment can be made, which contributes towards furthering our understanding of the photophysics of pyrene and towards locating the ideal spectral regions where to monitor this photo-response.

A further step forward was taken for simulating the non-linear spectra of azobenzene, another of the examples previously introduced. In this case the pump-probe spectrum was simulated, and the time-dependence during t_2 was included, being described using Pauli's master equation[49,54]

$$\dot{\rho_{ee}}(t) = -\sum_{e'} K_{e'e',ee}\rho_{e'e'}(t) \qquad (35)$$

where the elements of the K rate matrix correspond to population transfer rates among the involved excited ("pumped") states, evaluated on the basis of a 0K trajectory initiated in the S_2 $\pi\pi^*$ state (similarly to how it was done in pyrene above[48]) as well as including most of the remaining rates as the registered lifetimes extracted from experimental data. This allows computing the time-dependence of the different density matrix terms $\rho_{e'e'}(t)$ which are needed during t_2 to account for the population dynamics.

In this case we can describe the same ESA (within K_I) response term shown above for pyrene as

$$\begin{aligned} R_{ESA}^{(K_I)}(t_1,t_2,t_3) &= \left(\frac{i}{\hbar}\right)^3 \Theta(t_1)\Theta(t_2)\Theta(t_3)\sum_{ee}\left|\mu_{ge}\right|^2\left|\mu_{ef}\right|^2 \\ &\times e^{+i(\omega_{ge}-i\gamma_{eg})t_1 - i(\omega_{ee}-i\gamma_{ee})t_2 - i(\omega_{ef}-i\gamma_{fe})t_3} \\ &= \left(\frac{i}{\hbar}\right)^3 \Theta(t_1)\Theta(t_2)\Theta(t_3)\sum_{ee}\left|\mu_{ge}\right|^2\left|\mu_{ef}\right|^2 \\ &\times e^{+i(\omega_{ge}-i\tau_{ge}^{-1})t_1 - i(\omega_{ee}-i\tau_{ee}^{-1})t_2 - i\left(\omega_{ef}-i\tau_{ef}^{-1}\right)t_3 + \varphi_{fe}^{ESA}(t_1,t_2,t_3)} \end{aligned} \qquad (36)$$

where the first equality shows the development of the response function after applying the SOS approach, and the second depicts the development of the different dephasing terms into lifetimes plus a multipoint lineshape function term $\varphi_{fe}^{ESA}(t_1,t_2,t_3)$. One important point to make is that eq. 36 above is analogous to eq. 33 used in pyrene, except transition energies are denoted as ω_{ab} instead of energy differences and lifetimes are accounted for directly in τ_{ab}^{-1} instead of phenomenological rates Γ from eq. 20. $\varphi_{fe}^{ESA}(t_1,t_2,t_3)$ is quite complex and its concrete form depends on the specific phase-matching condition and Feynman diagram considered, the complete equations being provided elsewhere.[22,23,37]

Using these response contributions, the pump probe signal $W^{(3)}(t_2, \Omega_3)$ can be related to the general expression of the total third order signal $S^{(3)}(t_1, t_2, t_3)$ used in 2DES as

$$W^{(3)}(t_2, \Omega_3) = \int_{-\infty}^{\infty} dt_1 \int_{0}^{\infty} dt_3 S^{(3)}(t_1, t_2, t_3) e^{i\Omega_3 t_3} \delta(t_1) \qquad (37)$$

which represents a marginal of the Fourier-transformed signal, and neglects contributions between pulses τ_1 and τ_2, which are not resolved in pump-probe techniques. Moreover, the finite duration of the laser pulses was accounted for ad-hoc by convolving the pump-probe signal $W^{(3)}(t_2, \Omega_3)$ with a Gaussian function in the time domain

$$W^{(3)}(t_2, \Omega_3) = \int_{-\infty}^{\infty} d\tau \, W^{(3)}(\tau, \Omega_3) \cdot e^{\left(-\frac{(\tau - t_2)}{2\sigma^2}\right)} \qquad (38)$$

where $\sigma = 16$ fs was used to replicate the laser used in the experiment.[49]

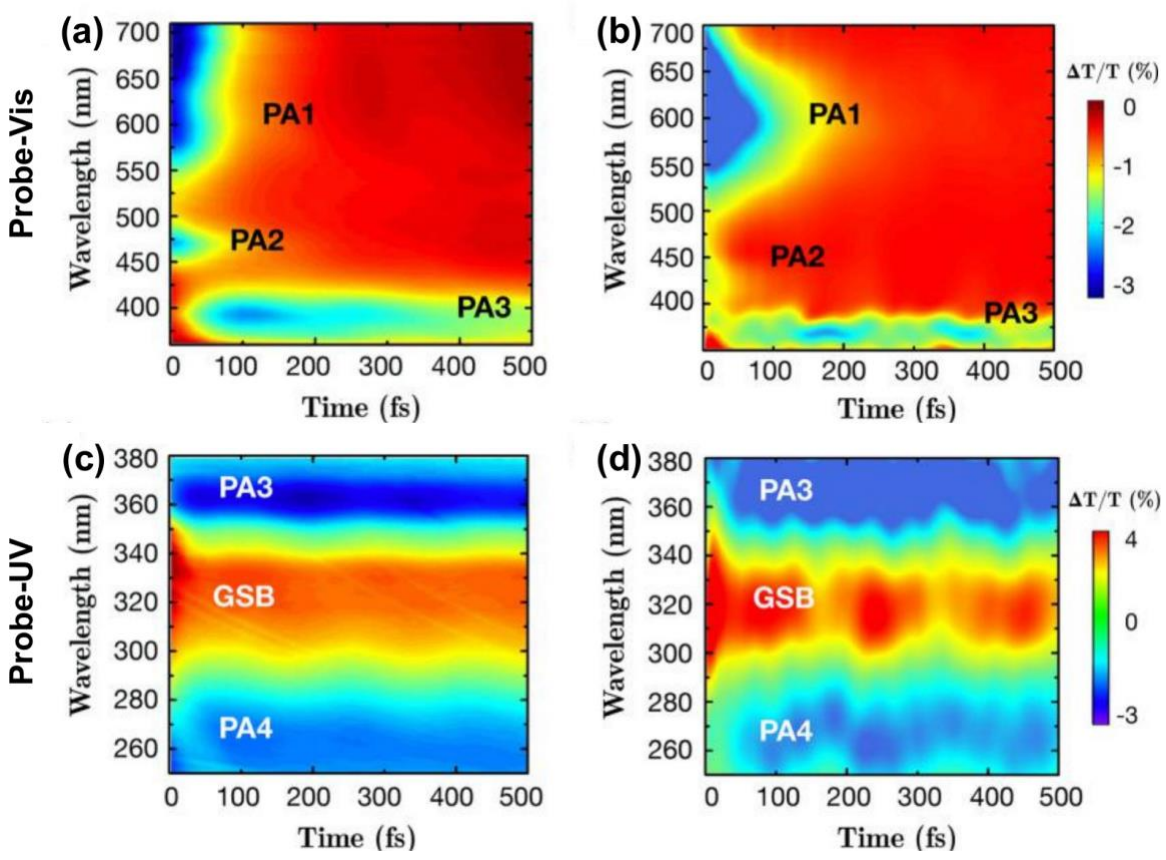

Figure 14. Experimental ((a) and (c); in ethanol) and theoretical ((b) and (d); gas-phase) pump-probe recorded signals in both Vis and UV spectral windows during the first 500 fs. Adapted from Ref. 49 with permission from the American Chemical Society.

Theoretical and experimental estimates are confronted in Fig. 14, where the above panels show the spectra while probing in the Vis energy window while the bottom panels refer to probe-UV energies. Left-hand side panels (a) and (c) are the experimentally recorded signals, while right-hand side panels (b) and (d) refer to the simulated spectra. PA signals refer to excited state photo-absorption (i.e., ESAs), and the colour scheme was given in this case with the opposite sign as the one above for pyrene (Fig. 13), i.e. ESAs are plotted as negative contributions in blue, while the GSB is positive in red. Multiple pump-probe experiments are plotted in a single figure by recording multiple t_2 measurements with ultrashort broadband laser pulses and fitting the signals together. This approach has also been used to reproduced pump-probe spectral signals of DNA based systems undergoing ultrafast deactivations, showing remarkable agreement with experiment.[121,122]

As can be seen, the lineshapes are approximately reproduced by theory, which is able to predict signals with similar shapes at the right spectral positions, as well as their time-dependence. Perhaps the most striking difference between theory and experiment is the overly coherent shape of the model: this is partly due to being based on a harmonic approximation such as the DBO, but it also reflects the limitations that may be observed experimentally due to temporal resolution. In this case it mostly shows overly harmonic behaviour which can faithfully describe the linear absorption signals shown in Fig. 5 but that encounters more challenges for appropriately describing non-linear features,[36,77,84] particularly when applied to a highly flexible system like azobenzene. Interestingly, the model shows an oscillatory pattern which was hard to see in the experiment, and which was used to ascribe a prominent role in deactivation to vibrational coherences that are easier to see in the UV window experimentally.

The methodologies for including solvent effects through the splitting of the spectral density shown above in Section 3.1.1 for adenine can also be applied to non-linear signals, both to pump-probe and 2DES, and the specific details can be consulted in Ref. 37.

[19.4.3.1 Time-resolved NEA approach to non-linear spectroscopy]

One last option we discuss for simulating time-resolved spectral signatures is to use a NEA-like approach whereby ESA and SE/GSB signals are simulated on top of a swarm of trajectories used in non-adiabatic molecular dynamics simulations, and broadened by phenomenological Gaussian functions. The advantage of this approach is its simplicity: the manifold of states and the transition dipole moments connecting them is all the information required per timestep, which can be easily obtained from electronic structure simulations.

Moreover, the unconstrained nature of on-the-fly trajectory-based schemes includes in part certain anharmonicity to the molecular motions which can be important for describing certain features. Despite this, the actual lineshapes are still described phenomenologically by ad-hoc broadened Gaussian functions, which may not be able to reproduce complex broadenings. This approach has also been used in the context of 2DES to predict how signals broaden in time.[102]

There are many examples of this kind of treatment in the literature:[92,93,123–126] perhaps the best-known case refers to the study on the photoisomerisation of Rhodopsin by Cerullo, Garavelli and co-workers,[124] and here we show how it can be applied to study ultrafast excited state dynamics such as those occurring in DNA/RNA excited state cations formed after vacuum-UV light exposure.[116,118]

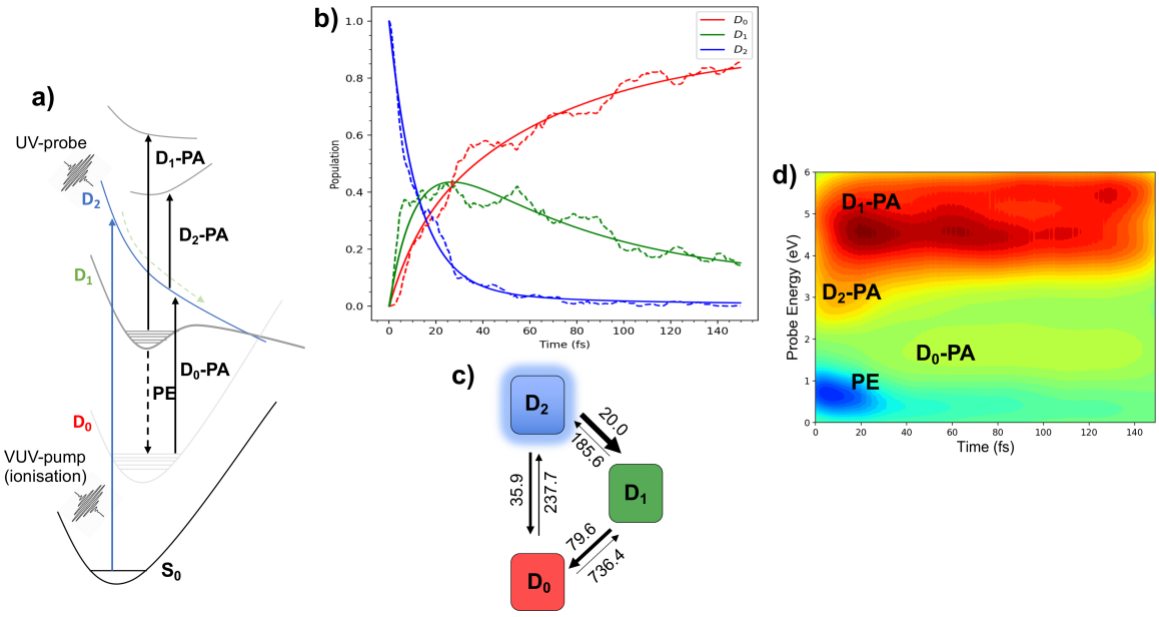

Figure 15. Excited state decay of cation uracil upon accessing the second cation excited state $D_2(^2\pi_{H\text{-}1}^{+})$. a) Diagram with the different potential energy surfaces involved in the photo-process, together with a scheme containing the different spectral signals used to rationalise the photo-process. b) Excited state populations resulting from Tully surface hopping simulations over 130 trajectories, dashed lines indicating the resulting populations while full lines denote the multistate kinetic model fitting. c) Kinetic model results after fitting all state populations, numbers referring to the estimated lifetimes

while the arrows' thickness denotes the fraction of trajectories following each pathway.

d) Simulated pump-probe spectra with the time-resolved NEA approach.

Figure 15 shows the simulated time-resolved pump-probe spectra for the uracil cation after accessing the cation second excited state $D_2(^2\pi_{H\text{-}1}{}^+)$.[118] Selection rules change in photoionisation: as a consequence, it is not straight-forward to know which is the initially accessed state. We here assume population to $D_2(^2\pi_{H\text{-}1}{}^+)$ as it allows discussing the different emerging spectral signals when accessing different states and how these types of simulations can be used to monitor photo-processes.

Upon accessing the D_2 state (Figure 15a), an ultrafast decay to the $D_1(^2n_{O}{}^+)$ state is predicted, which subsequently decays to the cation ground state $D_0(^2\pi_{H}{}^+)$, leading to a step-wise decay mechanism. An energy level scheme is provided together with the most important spectral fingerprints predicted for each state, and that will serve to distinguish the evolution of the wave packet along the excited-state deactivation.

This can be observed in the population decays (Figure 15b), where the pronounced decay of D_2 is concomitant with a rise of D_1 and D_0 populations, D_1 population being quickly funneled down to the D_0 ground state also in ultrafast timescales. The general reactivity can be extracted and analysed with a kinetic model like the one presented in Figure 15c, which uses the population decays to estimate lifetimes for the different processes, the thickness of the arrows representing the fraction of trajectories undergoing decay in each direction, while the associated numbers show the estimated lifetimes for that particular pathway. As can be seen, a very fast (~20 fs) $D_2 \rightarrow D_1$ decay is followed by a sub-100 fs $D_1 \rightarrow D_0$ population transfer, suggesting a sequential $D_2 \rightarrow D_1 \rightarrow D_0$ deactivation model to reach the cation ground state, even if a non-negligible amount of $D_2 \rightarrow D_0$ trajectories are also observed with a very short lifetime (~40 fs) featuring direct/concerted $D_2 \rightarrow D_0$ decay. To distinguish the different states populated along the dynamics, we apply the NEA scheme on top of multiple snapshots (one every ~1 fs) for each of the 130 trajectories propagated. This provides a time-resolved signal that is also broadened along time using a finite simulated laser pulse (in this case 20 fs, which is meant to predict measures from a set-up similar to Ref. 49). Applying this model results in a 2D map (Figure 15d) which shows probe energy vs time, red signals depicting ESA contributions while blue refers to SE. Quick inspection of Figure 15d shows the most clear and intense signal in the high end (~4.5 eV) of the probe energy spectrum rapidly emerges within 20 fs after population, and is associated to an ESA from the D_1 state labelled D_1-PA. This is in line with the population (Figure 15b) and kinetic model (Figure 15c) estimates, which point at a swift $D_2 \rightarrow D_1$ population transfer that is also observed in the D_2-PA signal that appears at early times (0 fs) and at ~3 eV energies, and which rapidly vanishes concomitantly with the $D_2 \rightarrow D_1$ ultrafast population transfer. After populating the D_1 state, a swift $D_1 \rightarrow D_0$ decay is predicted to follow, which is observed in the pump-probe simulated spectrum by the emerging D_0-PA signal at ~1.5 eV, as well as by the vast reduction in intensity of the D_1-PA fingerprint after ~100 fs as the D_1 population is almost depleted (~20%). D_0-PA appears

at delay times of 40 fs and longer, which is when the D_0 state is predicted to reach substantial (50%; see Figure 15b) population, and is represented by the $D_0 \rightarrow D_2$ ESA transition.

In this way we can see there are three distinctive spectral regions where we can observe signals appear and disappear depending on the specific state populated in time: ~3 eV for D_2-PA, ~4.5 eV for D_1-PA and ~1.5 eV for D_0-PA. These fingerprints, even if roughly estimated with the NEA approach, are well separated and should serve to differentiate the currently populated state in an experiment, thus providing a temporally resolved signal-to-state assignment that allows a more complete monitoring of the photo-reaction.

[19.5 Overview]

In this chapter we show different theoretical approaches to the simulation of linear and non-linear optical spectroscopies that use electronic structure easily obtained from popular commercial and open-source programs. We briefly introduce the basis of the Liouville space, a general approach to describe all kinds of spectroscopies applied in this case to the optical regime, and which offers a powerful venue to systematically include detail in the simulation of spectral signals. This is done by outlining different approximations, which can be applied for the simulation of both linear and non-linear experiments.

The SOS approach is used to expand the model onto the eigenvalues of the molecular Hamiltonian, which can then be combined with electronic structure data in the form of transition energies and transition dipole moments. The simplest models assume the delay time to be 0 and broadenings to arise due to phenomenological dephasings, and a connection is made with the popular NEA approach and the Gaussian broadening included therein. New and promising machine learning developments are shown whereby the NEA approach can be freed from this phenomenological broadening, leading to the GMM-NEA method that results in more accurate and less arbitrary absorption profiles: this approach is used to study the absorption and photoelectron spectra of gas-phase ethylene, the latter being computed with the GMM-NEA scheme for the first time.

A more complex approach based on lineshape functions arising from applying the cumulant expansion and a DBO model is introduced, which further requires ground state normal modes and vibrations (i.e., the Hessian) and electronic excited state gradients. This more complex methodology projects the ground state Hessian onto the excited states, therefore assuming the frequencies on all states to be the same but just displaced in position. The DBO model, which assumes the system to behave harmonically, is applied to simulate the linear absorption of pyrene, azobenzene and adenine, with different levels of sophistication. For pyrene, a single-trajectory molecular dynamics scheme is applied and the parameters along the dynamics fitted to a Fourier series, obtaining vibrationally

resolved spectra at two different temperatures where solvent contributions are switched off. In azobenzene, the normal modes and frequencies of the ground-state Hessian and displaced oscillators in the excited states are used to describe the complex lineshapes recorded experimentally with prominent vibronic progressions, even when considering multiple temperatures and where solvent contributions are included through a dephasing constant. Adenine is simulated taking into account both intramolecular and intermolecular interactions towards its lineshape broadening by splitting their contributions to the spectral density, leading to a realistic spectrum in water solution which is obtained from QM/MM simulations and that captures the band's asymmetry.

Different levels of sophistication are therefore applied within linear absorption, showing distinct performance: vibronic features appear to be better represented in pyrene compared to azobenzene, as the former is more rigid and thus fits better into the harmonic approximation adopted in DBO. Adenine, on the other hand, shows how the subtle effects introduced by solvation can be difficult and counter-intuitive to simulate. The electronic structure method employed for computing the energy gap fluctuation (auto/cross)-correlation functions needs to be accurate but also consistent under different solvation patterns, showing in this case a surprisingly better performance of the CASSCF method compared against the more correlated CASPT2.

Non-linear spectroscopies are initially introduced through the static approximation, which implies including broadenings completely phenomenologically through the use of ad-hoc dephasing constants. This technique is shown to be useful in the context of 2DES as it allows finding spectral regions where the main fingerprints will emerge. The example of gas-phase adenine is provided, showing the vast manifold of states accessible through ESAs in such systems and the significant differences in intensity observed for the L_a and L_b state, which allows segregating state-specific signals thanks to the extra Ω_1 dimension.

A NEA-based static approach is shown based on computing signals on top of excited state optimised structures. This rather simplistic model is applied to water-solvated uridine, showing remarkable similarities with the experiment and sufficing to enable a state-to-signal assignment that facilitates a qualitative molecular model for interpreting the recorded evidence.

The DBO model is applied to non-linear spectroscopies, particularly to the cases of pyrene and azobenzene. For pyrene, a single-trajectory approach is used to fit in the energy fluctuations and obtain the spectral density. The 2DES signals produced at both $t_2 = 0$ and $t_2 = 1$ ps show prominent vibrational progressions, the latter being in agreement with the available experimental evidence. In azobenzene, on the other hand, the ground state Hessian is used to construct the spectral density. Time-dependent pump-probe signals are computed including broadenings, leading to qualitative agreements with experiment. Even when simulating the simpler pump-probe, larger deviations are observed compared to those seen in pyrene for 2DES, which is due to the higher flexibility (i.e. anharmonicity) of azobenzene and that partly showcases potential limitations of the harmonic DBO model.

The last approach introduced uses a NEA-like scheme on top of multiple ensembles and along a swarm of excited state dynamics trajectories, assuming simple phenomenological Gaussian broadenings. By running over the swarm of trajectories, the signals are averaged and, despite its simplicity, this method is still able to show qualitative differences for the different active states along the ultrafast cation excited state decay of uracil. Even if lineshapes are beyond its scope, this approach has the advantage of running on unconstrained trajectories: this means it includes a certain degree of anharmonicity by construction, and it can thus be easily implemented coupled to popular semi-classical on-the-fly molecular dynamics schemes like trajectory surface hopping, making it suitable for studying highly anharmonic systems.

[Chapter References]

(1) Levine, Ira N. *Molecular Spectroscopy*; Wiley: New York, 1975.

(2) Nibbering, E. T. J.; Fidder, H.; Pines, E. ULTRAFAST CHEMISTRY: Using Time-Resolved Vibrational Spectroscopy for Interrogation of Structural Dynamics. *Annu. Rev. Phys. Chem.* **2005**, *56* (1), 337–367. https://doi.org/10.1146/annurev.physchem.56.092503.141314.

(3) Kukura, P.; McCamant, D. W.; Mathies, R. A. Femtosecond Stimulated Raman Spectroscopy. *Annu. Rev. Phys. Chem.* **2007**, *58* (1), 461–488. https://doi.org/10.1146/annurev.physchem.58.032806.104456.

(4) Mukamel, S. Femtosecond Optical Spectroscopy: A Direct Look at Elementary Chemical Events. *Annu. Rev. Phys. Chem.* **1990**, *41* (1), 647–681. https://doi.org/10.1146/annurev.pc.41.100190.003243.

(5) Henriksen, N. E.; Engel, V. Femtosecond Pump-Probe Spectroscopy: A Theoretical Analysis of Transient Signals and Their Relation to Nuclear Wave-Packet Motion. *International Reviews in Physical Chemistry* **2001**, *20* (2), 93–126. https://doi.org/10.1080/01442350010028523.

(6) Scholes, G. D.; Fleming, G. R.; Chen, L. X.; Aspuru-Guzik, A.; Buchleitner, A.; Coker, D. F.; Engel, G. S.; van Grondelle, R.; Ishizaki, A.; Jonas, D. M.; Lundeen, J. S.; McCusker, J. K.; Mukamel, S.; Ogilvie, J. P.; Olaya-Castro, A.; Ratner, M. A.; Spano, F. C.; Whaley, K. B.; Zhu, X. Using Coherence to Enhance Function in Chemical and Biophysical Systems. *Nature* **2017**, *543* (7647), 647–656. https://doi.org/10.1038/nature21425.

(7) Rosker, M. J.; Dantus, M.; Zewail, A. H. Femtosecond Clocking of the Chemical Bond. *Science* **1988**, *241* (4870), 1200–1202. https://doi.org/10.1126/science.241.4870.1200.

(8) Kohler, B.; Krause, J. L.; Raksi, F.; Wilson, K. R.; Yakovlev, V. V.; Whitnell, R. M.; Yan, Y. Controlling the Future of Matter. *Acc. Chem. Res.* **1995**, *28* (3), 133–140. https://doi.org/10.1021/ar00051a006.

(9) Polanyi, J. C.; Zewail, A. H. Direct Observation of the Transition State. *Acc. Chem. Res.* **1995**, *28* (3), 119–132. https://doi.org/10.1021/ar00051a005.

(10) Zewail, A. H. Femtochemistry: Atomic-Scale Dynamics of the Chemical Bond †. *J. Phys. Chem. A* **2000**, *104* (24), 5660–5694. https://doi.org/10.1021/jp001460h.

(11) Carlson, T. A. Photoelectron Spectroscopy. *Annu. Rev. Phys. Chem.* **1975**, *26* (1), 211–234. https://doi.org/10.1146/annurev.pc.26.100175.001235.
(12) Schuurman, M. S.; Blanchet, V. Time-Resolved Photoelectron Spectroscopy: The Continuing Evolution of a Mature Technique. *Phys. Chem. Chem. Phys.* **2022**, 10.1039.D1CP05885A. https://doi.org/10.1039/D1CP05885A.
(13) Fielding, H. H.; Worth, G. A. Using Time-Resolved Photoelectron Spectroscopy to Unravel the Electronic Relaxation Dynamics of Photoexcited Molecules. *Chem. Soc. Rev.* **2018**, *47* (2), 309–321. https://doi.org/10.1039/C7CS00627F.
(14) Borrego-Varillas, R.; Nenov, A.; Ganzer, L.; Oriana, A.; Manzoni, C.; Tolomelli, A.; Rivalta, I.; Mukamel, S.; Garavelli, M.; Cerullo, G. Two-Dimensional UV Spectroscopy: A New Insight into the Structure and Dynamics of Biomolecules. *Chem. Sci.* **2019**, *10* (43), 9907–9921. https://doi.org/10.1039/C9SC03871J.
(15) Biswas, S.; Kim, J.; Zhang, X.; Scholes, G. D. Coherent Two-Dimensional and Broadband Electronic Spectroscopies. *Chem. Rev.* **2022**, *122* (3), 4257–4321. https://doi.org/10.1021/acs.chemrev.1c00623.
(16) Mandal, A.; Schultz, J. D.; Wu, Y.-L.; Coleman, A. F.; Young, R. M.; Wasielewski, M. R. Transient Two-Dimensional Electronic Spectroscopy: Coherent Dynamics at Arbitrary Times along the Reaction Coordinate. *J. Phys. Chem. Lett.* **2019**, *10* (13), 3509–3515. https://doi.org/10.1021/acs.jpclett.9b00826.
(17) Fuller, F. D.; Ogilvie, J. P. Experimental Implementations of Two-Dimensional Fourier Transform Electronic Spectroscopy. *Annu. Rev. Phys. Chem.* **2015**, *66* (1), 667–690. https://doi.org/10.1146/annurev-physchem-040513-103623.
(18) Maiuri, M.; Garavelli, M.; Cerullo, G. Ultrafast Spectroscopy: State of the Art and Open Challenges. *J. Am. Chem. Soc.* **2020**, *142* (1), 3–15. https://doi.org/10.1021/jacs.9b10533.
(19) Segarra-Martí, J.; Mukamel, S.; Garavelli, M.; Nenov, A.; Rivalta, I. Towards Accurate Simulation of Two-Dimensional Electronic Spectroscopy. *Top Curr Chem (Z)* **2018**, *376* (3), 24. https://doi.org/10.1007/s41061-018-0201-8.
(20) Engel, G. S.; Calhoun, T. R.; Read, E. L.; Ahn, T.-K.; Mančal, T.; Cheng, Y.-C.; Blankenship, R. E.; Fleming, G. R. Evidence for Wavelike Energy Transfer through Quantum Coherence in Photosynthetic Systems. *Nature* **2007**, *446* (7137), 782–786. https://doi.org/10.1038/nature05678.
(21) Olaya-Castro, A.; Scholes, G. D. Energy Transfer from Förster–Dexter Theory to Quantum Coherent Light-Harvesting. *International Reviews in Physical Chemistry* **2011**, *30* (1), 49–77. https://doi.org/10.1080/0144235X.2010.537060.
(22) Mukamel, Shaul. *Principles of Nonlinear Optical Spectroscopy*; Oxford Series on Optical and Imaging Sciences; Oxford University Press, 1999.
(23) Abramavicius, D.; Palmieri, B.; Voronine, D. V.; Šanda, F.; Mukamel, S. Coherent Multidimensional Optical Spectroscopy of Excitons in Molecular Aggregates; Quasiparticle versus Supermolecule Perspectives. *Chem. Rev.* **2009**, *109* (6), 2350–2408. https://doi.org/10.1021/cr800268n.
(24) Rivalta, I.; Nenov, A.; Cerullo, G.; Mukamel, S.; Garavelli, M. Ab Initio Simulations of Two-Dimensional Electronic Spectra: The SOS//QM/MM Approach. *Int. J. Quantum Chem.* **2014**, *114* (2), 85–93. https://doi.org/10.1002/qua.24511.

(25) Richter, M.; Fingerhut, B. P. Simulation of Multi-Dimensional Signals in the Optical Domain: Quantum-Classical Feedback in Nonlinear Exciton Propagation. *J. Chem. Theory Comput.* **2016**, *12* (7), 3284–3294. https://doi.org/10.1021/acs.jctc.6b00371.
(26) Kowalewski, M.; Fingerhut, B. P.; Dorfman, K. E.; Bennett, K.; Mukamel, S. Simulating Coherent Multidimensional Spectroscopy of Nonadiabatic Molecular Processes: From the Infrared to the X-Ray Regime. *Chem. Rev.* **2017**, *117* (19), 12165–12226. https://doi.org/10.1021/acs.chemrev.7b00081.
(27) Gelin, M. F.; Huang, X.; Xie, W.; Chen, L.; Došlić, N.; Domcke, W. Ab Initio Surface-Hopping Simulation of Femtosecond Transient-Absorption Pump–Probe Signals of Nonadiabatic Excited-State Dynamics Using the Doorway–Window Representation. *J. Chem. Theory Comput.* **2021**, acs.jctc.1c00109. https://doi.org/10.1021/acs.jctc.1c00109.
(28) Gelin, M. F.; Egorova, D.; Domcke, W. Efficient Calculation of Time- and Frequency-Resolved Four-Wave-Mixing Signals. *Acc. Chem. Res.* **2009**, *42* (9), 1290–1298. https://doi.org/10.1021/ar900045d.
(29) Segatta, F.; Nenov, A.; Nascimento, D. R.; Govind, N.; Mukamel, S.; Garavelli, M. ıSPECTRON : A Simulation Interface for Linear and Nonlinear Spectra with Ab-initio Quantum Chemistry Software. *J Comput Chem* **2021**, *42* (9), 644–659. https://doi.org/10.1002/jcc.26485.
(30) Crespo-Otero, R.; Barbatti, M. Recent Advances and Perspectives on Nonadiabatic Mixed Quantum–Classical Dynamics. *Chem. Rev.* **2018**, *118* (15), 7026–7068. https://doi.org/10.1021/acs.chemrev.7b00577.
(31) Mai, S.; Marquetand, P.; González, L. A General Method to Describe Intersystem Crossing Dynamics in Trajectory Surface Hopping. *Int. J. Quantum Chem.* **2015**, *115* (18), 1215–1231. https://doi.org/10.1002/qua.24891.
(32) Subotnik, J. E.; Jain, A.; Landry, B.; Petit, A.; Ouyang, W.; Bellonzi, N. Understanding the Surface Hopping View of Electronic Transitions and Decoherence. *Annu. Rev. Phys. Chem.* **2016**, *67* (1), 387–417. https://doi.org/10.1146/annurev-physchem-040215-112245.
(33) Curchod, B. F. E.; Martínez, T. J. Ab Initio Nonadiabatic Quantum Molecular Dynamics. *Chem. Rev.* **2018**, *118* (7), 3305–3336. https://doi.org/10.1021/acs.chemrev.7b00423.
(34) Richings, G. W.; Polyak, I.; Spinlove, K. E.; Worth, G. A.; Burghardt, I.; Lasorne, B. Quantum Dynamics Simulations Using Gaussian Wavepackets: The VMCG Method. *International Reviews in Physical Chemistry* **2015**, *34* (2), 269–308. https://doi.org/10.1080/0144235X.2015.1051354.
(35) Worth, G. A.; Cederbaum, L. S. BEYOND BORN-OPPENHEIMER: Molecular Dynamics Through a Conical Intersection. *Annu. Rev. Phys. Chem.* **2004**, *55* (1), 127–158. https://doi.org/10.1146/annurev.physchem.55.091602.094335.
(36) Zuehlsdorff, T. J.; Shedge, S. V.; Lu, S.-Y.; Hong, H.; Aguirre, V. P.; Shi, L.; Isborn, C. M. Vibronic and Environmental Effects in Simulations of Optical Spectroscopy. *Annu. Rev. Phys. Chem.* **2021**, *72* (1), 165–188. https://doi.org/10.1146/annurev-physchem-090419-051350.
(37) Segarra-Martí, J.; Segatta, F.; Mackenzie, T. A.; Nenov, A.; Rivalta, I.; Bearpark, M. J.; Garavelli, M. Modeling Multidimensional Spectral Lineshapes from First

Principles: Application to Water-Solvated Adenine. *Faraday Discuss.* **2020**, *221*, 219–244. https://doi.org/10.1039/C9FD00072K.
(38) Lee, M. K.; Huo, P.; Coker, D. F. Semiclassical Path Integral Dynamics: Photosynthetic Energy Transfer with Realistic Environment Interactions. *Annu. Rev. Phys. Chem.* **2016**, *67* (1), 639–668. https://doi.org/10.1146/annurev-physchem-040215-112252.
(39) Tanimura, Y. Stochastic Liouville, Langevin, Fokker–Planck, and Master Equation Approaches to Quantum Dissipative Systems. *J. Phys. Soc. Jpn.* **2006**, *75* (8), 082001. https://doi.org/10.1143/JPSJ.75.082001.
(40) Zimmermann, T.; Vaníček, J. Efficient On-the-Fly *Ab Initio* Semiclassical Method for Computing Time-Resolved Nonadiabatic Electronic Spectra with Surface Hopping or Ehrenfest Dynamics. *The Journal of Chemical Physics* **2014**, *141* (13), 134102. https://doi.org/10.1063/1.4896735.
(41) Tempelaar, R.; van der Vegte, C. P.; Knoester, J.; Jansen, T. L. C. Surface Hopping Modeling of Two-Dimensional Spectra. *The Journal of Chemical Physics* **2013**, *138* (16), 164106. https://doi.org/10.1063/1.4801519.
(42) Petit, A. S.; Subotnik, J. E. Calculating Time-Resolved Differential Absorbance Spectra for Ultrafast Pump-Probe Experiments with Surface Hopping Trajectories. *The Journal of Chemical Physics* **2014**, *141* (15), 154108. https://doi.org/10.1063/1.4897258.
(43) Begušić, T.; Vaníček, J. Finite-Temperature, Anharmonicity, and Duschinsky Effects on the Two-Dimensional Electronic Spectra from Ab Initio Thermo-Field Gaussian Wavepacket Dynamics. *J. Phys. Chem. Lett.* **2021**, *12* (11), 2997–3005. https://doi.org/10.1021/acs.jpclett.1c00123.
(44) Begušić, T.; Vaníček, J. On-the-Fly *Ab Initio* Semiclassical Evaluation of Third-Order Response Functions for Two-Dimensional Electronic Spectroscopy. *J. Chem. Phys.* **2020**, *153* (18), 184110. https://doi.org/10.1063/5.0031216.
(45) Begušić, T.; Roulet, J.; Vaníček, J. On-the-Fly *Ab Initio* Semiclassical Evaluation of Time-Resolved Electronic Spectra. *J. Chem. Phys.* **2018**, *149* (24), 244115. https://doi.org/10.1063/1.5054586.
(46) Mukamel, S. Nonimpact Unified Theory of Four-Wave Mixing and Two-Photon Processes. *Phys. Rev. A* **1983**, *28* (6), 3480–3492. https://doi.org/10.1103/PhysRevA.28.3480.
(47) Abramavicius, D.; Valkunas, L.; Mukamel, S. Transport and Correlated Fluctuations in the Nonlinear Optical Response of Excitons. *Europhys. Lett.* **2007**, *80* (1), 17005. https://doi.org/10.1209/0295-5075/80/17005.
(48) Nenov, A.; Giussani, A.; Fingerhut, B. P.; Rivalta, I.; Dumont, E.; Mukamel, S.; Garavelli, M. Spectral Lineshapes in Nonlinear Electronic Spectroscopy. *Phys. Chem. Chem. Phys.* **2015**, *17* (46), 30925–30936. https://doi.org/10.1039/C5CP01167A.
(49) Nenov, A.; Borrego-Varillas, R.; Oriana, A.; Ganzer, L.; Segatta, F.; Conti, I.; Segarra-Marti, J.; Omachi, J.; Dapor, M.; Taioli, S.; Manzoni, C.; Mukamel, S.; Cerullo, G.; Garavelli, M. UV-Light-Induced Vibrational Coherences: The Key to Understand Kasha Rule Violation in Trans-Azobenzene. *J Phys Chem Lett* **2018**, *9* (7), 1534–1541. https://doi.org/10.1021/acs.jpclett.8b00152.

(50) Li, B.; Johnson, A. E.; Mukamel, S.; Myers, A. B. The Brownian Oscillator Model for Solvation Effects in Spontaneous Light Emission and Their Relationship to Electron Transfer. *J. Am. Chem. Soc.* **1994**, *116* (24), 11039–11047. https://doi.org/10.1021/ja00103a020.
(51) Butkus, V.; Valkunas, L.; Abramavicius, D. Molecular Vibrations-Induced Quantum Beats in Two-Dimensional Electronic Spectroscopy. *The Journal of Chemical Physics* **2012**, *137* (4), 044513. https://doi.org/10.1063/1.4737843.
(52) Zuehlsdorff, T. J.; Hong, H.; Shi, L.; Isborn, C. M. Nonlinear Spectroscopy in the Condensed Phase: The Role of Duschinsky Rotations and Third Order Cumulant Contributions. *J. Chem. Phys.* **2020**, *153* (4), 044127. https://doi.org/10.1063/5.0013739.
(53) Valkunas, L.; Abramavicius, D.; Mančal, T. *Molecular Excitation Dynamics and Relaxation: VALKUNAS:MOLECULAR EXCITATION DYNAMICS AND RELAXATION O-BK*; Wiley-VCH Verlag GmbH & Co. KGaA: Weinheim, Germany, 2013. https://doi.org/10.1002/9783527653652.
(54) Picchiotti, A.; Nenov, A.; Giussani, A.; Prokhorenko, V. I.; Miller, R. J. D.; Mukamel, S.; Garavelli, M. Pyrene, a Test Case for Deep-Ultraviolet Molecular Photophysics. *J. Phys. Chem. Lett.* **2019**, *10* (12), 3481–3487. https://doi.org/10.1021/acs.jpclett.9b01325.
(55) Marcus, R. A. On the Theory of Oxidation-Reduction Reactions Involving Electron Transfer. I. *The Journal of Chemical Physics* **1956**, *24* (5), 966–978. https://doi.org/10.1063/1.1742723.
(56) Shedge, S. V.; Zuehlsdorff, T. J.; Khanna, A.; Conley, S.; Isborn, C. M. Explicit Environmental and Vibronic Effects in Simulations of Linear and Nonlinear Optical Spectroscopy. *J. Chem. Phys.* **2021**, *154* (8), 084116. https://doi.org/10.1063/5.0038196.
(57) Chen, M. S.; Zuehlsdorff, T. J.; Morawietz, T.; Isborn, C. M.; Markland, T. E. Exploiting Machine Learning to Efficiently Predict Multidimensional Optical Spectra in Complex Environments. *J. Phys. Chem. Lett.* **2020**, *11* (18), 7559–7568. https://doi.org/10.1021/acs.jpclett.0c02168.
(58) Segatta, F.; Cupellini, L.; Jurinovich, S.; Mukamel, S.; Dapor, M.; Taioli, S.; Garavelli, M.; Mennucci, B. A Quantum Chemical Interpretation of Two-Dimensional Electronic Spectroscopy of Light-Harvesting Complexes. *J. Am. Chem. Soc.* **2017**, *139* (22), 7558–7567. https://doi.org/10.1021/jacs.7b02130.
(59) Segatta, F.; Cupellini, L.; Garavelli, M.; Mennucci, B. Quantum Chemical Modeling of the Photoinduced Activity of Multichromophoric Biosystems: Focus Review. *Chem. Rev.* **2019**, *119* (16), 9361–9380. https://doi.org/10.1021/acs.chemrev.9b00135.
(60) Valleau, S.; Eisfeld, A.; Aspuru-Guzik, A. On the Alternatives for Bath Correlators and Spectral Densities from Mixed Quantum-Classical Simulations. *The Journal of Chemical Physics* **2012**, *137* (22), 224103. https://doi.org/10.1063/1.4769079.
(61) Bozovic, O.; Jankovic, B.; Hamm, P. Using Azobenzene Photocontrol to Set Proteins in Motion. *Nat Rev Chem* **2022**, *6* (2), 112–124. https://doi.org/10.1038/s41570-021-00338-6.

(62) Merritt, I. C. D.; Jacquemin, D.; Vacher, M. *Cis → Trans* Photoisomerisation of Azobenzene: A Fresh Theoretical Look. *Phys. Chem. Chem. Phys.* **2021**, *23* (35), 19155–19165. https://doi.org/10.1039/D1CP01873F.
(63) Rau, H. Photoisomerization of Azobenzenes. In *Photochemistry and Photophysics*; CRC Press, Inc.: Corporate Blvd., N. W., Boca Raton, Florida, 33431, 1989; Vol. 2.
(64) Dyck, R. H.; McClure, D. S. Ultraviolet Spectra of Stilbene, *p* -Monohalogen Stilbenes, and Azobenzene and the *Trans* to *Cis* Photoisomerization Process. *The Journal of Chemical Physics* **1962**, *36* (9), 2326–2345. https://doi.org/10.1063/1.1732885.
(65) Schwarz, F. P.; Wasik, S. P. Fluorescence Measurements of Benzene, Naphthalene, Anthracene, Pyrene, Fluoranthene, and Benzo[e]Pyrene in Water. *Anal. Chem.* **1976**, *48* (3), 524–528. https://doi.org/10.1021/ac60367a046.
(66) Halasinski, T. M.; Salama, F.; Allamandola, L. J. Investigation of the Ultraviolet, Visible, and Near-Infrared Absorption Spectra of Hydrogenated Polycyclic Aromatic Hydrocarbons and Their Cations. *ApJ* **2005**, *628* (1), 555–566. https://doi.org/10.1086/430631.
(67) Nenov, A.; Giussani, A.; Segarra-Martí, J.; Jaiswal, V. K.; Rivalta, I.; Cerullo, G.; Mukamel, S.; Garavelli, M. Modeling the High-Energy Electronic State Manifold of Adenine: Calibration for Nonlinear Electronic Spectroscopy. *The Journal of Chemical Physics* **2015**, *142* (21), 212443. https://doi.org/10.1063/1.4921016.
(68) Segarra-Martí, J.; Jaiswal, V. K.; Pepino, A. J.; Giussani, A.; Nenov, A.; Mukamel, S.; Garavelli, M.; Rivalta, I. Two-Dimensional Electronic Spectroscopy as a Tool for Tracking Molecular Conformations in DNA/RNA Aggregates. *Faraday Discuss.* **2018**, *207*, 233–250. https://doi.org/10.1039/C7FD00201G.
(69) Middleton, C. T.; de La Harpe, K.; Su, C.; Law, Y. K.; Crespo-Hernández, C. E.; Kohler, B. DNA Excited-State Dynamics: From Single Bases to the Double Helix. *Annu Rev Phys Chem* **2009**, *60*, 217–239. https://doi.org/10.1146/annurev.physchem.59.032607.093719.
(70) Borrego-Varillas, R.; Cerullo, G.; Markovitsi, D. Exciton Trapping Dynamics in DNA Multimers. *J. Phys. Chem. Lett.* **2019**, *10* (7), 1639–1643. https://doi.org/10.1021/acs.jpclett.9b00450.
(71) Martínez-Fernández, L.; Pepino, A. J.; Segarra-Martí, J.; Jovaišaitė, J.; Vaya, I.; Nenov, A.; Markovitsi, D.; Gustavsson, T.; Banyasz, A.; Garavelli, M.; Improta, R. Photophysics of Deoxycytidine and 5-Methyldeoxycytidine in Solution: A Comprehensive Picture by Quantum Mechanical Calculations and Femtosecond Fluorescence Spectroscopy. *J. Am. Chem. Soc.* **2017**, *139* (23), 7780–7791. https://doi.org/10.1021/jacs.7b01145.
(72) Giussani, A.; Segarra-Martí, J.; Nenov, A.; Rivalta, I.; Tolomelli, A.; Mukamel, S.; Garavelli, M. Spectroscopic Fingerprints of DNA/RNA Pyrimidine Nucleobases in Third-Order Nonlinear Electronic Spectra. *Theor Chem Acc* **2016**, *135* (5), 121. https://doi.org/10.1007/s00214-016-1867-z.
(73) Segarra-Martí, J.; Pepino, A. J.; Nenov, A.; Mukamel, S.; Garavelli, M.; Rivalta, I. The Highly Excited-State Manifold of Guanine: Calibration for Nonlinear Electronic Spectroscopy Simulations. *Theor Chem Acc* **2018**, *137* (3), 47. https://doi.org/10.1007/s00214-018-2225-0.

(74) Segarra-Martí, J.; Zvereva, E.; Marazzi, M.; Brazard, J.; Dumont, E.; Assfeld, X.; Haacke, S.; Garavelli, M.; Monari, A.; Léonard, J.; Rivalta, I. Resolving the Singlet Excited State Manifold of Benzophenone by First-Principles Simulations and Ultrafast Spectroscopy. *J Chem Theory Comput* **2018**, *14* (5), 2570–2585. https://doi.org/10.1021/acs.jctc.7b01208.
(75) Crespo-Otero, R.; Barbatti, M. Spectrum Simulation and Decomposition with Nuclear Ensemble: Formal Derivation and Application to Benzene, Furan and 2-Phenylfuran. In *Marco Antonio Chaer Nascimento*; Ornellas, F. R., João Ramos, M., Eds.; Highlights in Theoretical Chemistry; Springer Berlin Heidelberg: Berlin, Heidelberg, 2014; Vol. 4, pp 89–102. https://doi.org/10.1007/978-3-642-41163-2_9.
(76) Arbelo-González, W.; Crespo-Otero, R.; Barbatti, M. Steady and Time-Resolved Photoelectron Spectra Based on Nuclear Ensembles. *J. Chem. Theory Comput.* **2016**, *12* (10), 5037–5049. https://doi.org/10.1021/acs.jctc.6b00704.
(77) Zuehlsdorff, T. J.; Hong, H.; Shi, L.; Isborn, C. M. Influence of Electronic Polarization on the Spectral Density. *J. Phys. Chem. B* **2020**, *124* (3), 531–543. https://doi.org/10.1021/acs.jpcb.9b10250.
(78) Xue, B.-X.; Barbatti, M.; Dral, P. O. Machine Learning for Absorption Cross Sections. *J Phys Chem A* **2020**, *124* (35), 7199–7210. https://doi.org/10.1021/acs.jpca.0c05310.
(79) Cerdán, L.; Roca-Sanjuán, D. Reconstruction of Nuclear Ensemble Approach Electronic Spectra Using Probabilistic Machine Learning. *J. Chem. Theory Comput.* **2022**, *18* (5), 3052–3064. https://doi.org/10.1021/acs.jctc.2c00004.
(80) Mintz, D. M.; Kuppermann, A. Photoelectron Spectroscopy of Ethylene, Isobutylene, Trimethylethylene, and Tetramethylethylene at Variable Angle. *The Journal of Chemical Physics* **1979**, *71* (8), 3499–3513. https://doi.org/10.1063/1.438739.
(81) Hazra, A.; Chang, H. H.; Nooijen, M. First Principles Simulation of the UV Absorption Spectrum of Ethylene Using the Vertical Franck-Condon Approach. *The Journal of Chemical Physics* **2004**, *121* (5), 2125–2136. https://doi.org/10.1063/1.1768173.
(82) Melania Oana, C.; Krylov, A. I. Dyson Orbitals for Ionization from the Ground and Electronically Excited States within Equation-of-Motion Coupled-Cluster Formalism: Theory, Implementation, and Examples. *The Journal of Chemical Physics* **2007**, *127* (23), 234106. https://doi.org/10.1063/1.2805393.
(83) Krylov, A. I. From Orbitals to Observables and Back. *J. Chem. Phys.* **2020**, *153* (8), 080901. https://doi.org/10.1063/5.0018597.
(84) Abou Taka, A.; Lu, S.-Y.; Gowland, D.; Zuehlsdorff, T. J.; Corzo, H. H.; Pribram-Jones, A.; Shi, L.; Hratchian, H. P.; Isborn, C. M. Comparison of Linear Response Theory, Projected Initial Maximum Overlap Method, and Molecular Dynamics-Based Vibronic Spectra: The Case of Methylene Blue. *J. Chem. Theory Comput.* **2022**, acs.jctc.1c01127. https://doi.org/10.1021/acs.jctc.1c01127.
(85) Maiuri, M.; Brazard, J. Electronic Couplings in (Bio-) Chemical Processes. *Top Curr Chem (Z)* **2018**, *376* (2), 10. https://doi.org/10.1007/s41061-017-0180-1.

(86) Jonas, D. M. Two-Dimensional Femtosecond Spectroscopy. *Annu. Rev. Phys. Chem.* **2003**, *54* (1), 425–463. https://doi.org/10.1146/annurev.physchem.54.011002.103907.
(87) Mukamel, S. Multidimensional Femtosecond Correlation Spectroscopies of Electronic and Vibrational Excitations. *Annu. Rev. Phys. Chem.* **2000**, *51* (1), 691–729. https://doi.org/10.1146/annurev.physchem.51.1.691.
(88) Brańczyk, A. M.; Turner, D. B.; Scholes, G. D. Crossing Disciplines - A View on Two-Dimensional Optical Spectroscopy: Crossing Disciplines - A View on Two-Dimensional Optical Spectroscopy. *ANNALEN DER PHYSIK* **2014**, *526* (1–2), 31–49. https://doi.org/10.1002/andp.201300153.
(89) Jonas, D. M. Vibrational and Nonadiabatic Coherence in 2D Electronic Spectroscopy, the Jahn–Teller Effect, and Energy Transfer. *Annu. Rev. Phys. Chem.* **2018**, *69* (1), 327–352. https://doi.org/10.1146/annurev-physchem-052516-050602.
(90) Nenov, A.; Rivalta, I.; Cerullo, G.; Mukamel, S.; Garavelli, M. Disentangling Peptide Configurations via Two-Dimensional Electronic Spectroscopy: Ab Initio Simulations Beyond the Frenkel Exciton Hamiltonian. *J. Phys. Chem. Lett.* **2014**, *5* (4), 767–771. https://doi.org/10.1021/jz5002314.
(91) Ruckenbauer, M.; Mai, S.; Marquetand, P.; González, L. Photoelectron Spectra of 2-Thiouracil, 4-Thiouracil, and 2,4-Dithiouracil. *J Chem Phys* **2016**, *144* (7), 074303. https://doi.org/10.1063/1.4941948.
(92) Ruckenbauer, M.; Mai, S.; Marquetand, P.; González, L. Revealing Deactivation Pathways Hidden in Time-Resolved Photoelectron Spectra. *Sci Rep* **2016**, *6* (1), 35522. https://doi.org/10.1038/srep35522.
(93) Mai, S.; Mohamadzade, A.; Marquetand, P.; González, L.; Ullrich, S. Simulated and Experimental Time-Resolved Photoelectron Spectra of the Intersystem Crossing Dynamics in 2-Thiouracil. *Molecules* **2018**, *23* (11), 2836. https://doi.org/10.3390/molecules23112836.
(94) Hudock, H. R.; Levine, B. G.; Thompson, A. L.; Satzger, H.; Townsend, D.; Gador, N.; Ullrich, S.; Stolow, A.; Martínez, T. J. Ab Initio Molecular Dynamics and Time-Resolved Photoelectron Spectroscopy of Electronically Excited Uracil and Thymine. *J. Phys. Chem. A* **2007**, *111* (34), 8500–8508. https://doi.org/10.1021/jp0723665.
(95) Bennett, K.; Kowalewski, M.; Mukamel, S. Nonadiabatic Dynamics May Be Probed through Electronic Coherence in Time-Resolved Photoelectron Spectroscopy. *J. Chem. Theory Comput.* **2016**, *12* (2), 740–752. https://doi.org/10.1021/acs.jctc.5b00824.
(96) Jadoun, D.; Kowalewski, M. Time-Resolved Photoelectron Spectroscopy of Conical Intersections with Attosecond Pulse Trains. *J. Phys. Chem. Lett.* **2021**, *12* (33), 8103–8108. https://doi.org/10.1021/acs.jpclett.1c01843.
(97) Cavaletto, S. M.; Keefer, D.; Mukamel, S. Electronic Coherences in Nonadiabatic Molecular Photophysics Revealed by Time-Resolved Photoelectron Spectroscopy. *Proc. Natl. Acad. Sci. U.S.A.* **2022**, *119* (11), e2121383119. https://doi.org/10.1073/pnas.2121383119.
(98) Conti, I.; Cerullo, G.; Nenov, A.; Garavelli, M. Ultrafast Spectroscopy of Photoactive Molecular Systems from First Principles: Where We Stand Today and

Where We Are Going. *J. Am. Chem. Soc.* **2020**, *142* (38), 16117–16139. https://doi.org/10.1021/jacs.0c04952.
(99) Nuernberger, P.; Ruetzel, S.; Brixner, T. Multidimensional Electronic Spectroscopy of Photochemical Reactions. *Angew. Chem. Int. Ed.* **2015**, *54* (39), 11368–11386. https://doi.org/10.1002/anie.201502974.
(100) Nenov, A.; Segarra-Martí, J.; Giussani, A.; Conti, I.; Rivalta, I.; Dumont, E.; Jaiswal, V. K.; Altavilla, S. F.; Mukamel, S.; Garavelli, M. Probing Deactivation Pathways of DNA Nucleobases by Two-Dimensional Electronic Spectroscopy: First Principles Simulations. *Faraday Discuss.* **2015**, *177*, 345–362. https://doi.org/10.1039/C4FD00175C.
(101) Li, Q.; Giussani, A.; Segarra-Martí, J.; Nenov, A.; Rivalta, I.; Voityuk, A. A.; Mukamel, S.; Roca-Sanjuán, D.; Garavelli, M.; Blancafort, L. Multiple Decay Mechanisms and 2D-UV Spectroscopic Fingerprints of Singlet Excited Solvated Adenine-Uracil Monophosphate. *Chemistry* **2016**, *22* (22), 7497–7507. https://doi.org/10.1002/chem.201505086.
(102) Zvereva, E.; Segarra-Martí, J.; Marazzi, M.; Brazard, J.; Nenov, A.; Weingart, O.; Léonard, J.; Garavelli, M.; Rivalta, I.; Dumont, E.; Assfeld, X.; Haacke, S.; Monari, A. The Effect of Solvent Relaxation in the Ultrafast Time-Resolved Spectroscopy of Solvated Benzophenone. *Photochem. Photobiol. Sci.* **2018**, *17* (3), 323–331. https://doi.org/10.1039/C7PP00439G.
(103) Giussani, A.; Marcheselli, J.; Mukamel, S.; Garavelli, M.; Nenov, A. On the Simulation of Two-dimensional Electronic Spectroscopy of Indole-containing Peptides. *Photochem Photobiol* **2017**, *93* (6), 1368–1380. https://doi.org/10.1111/php.12770.
(104) Nenov, A.; Rivalta, I.; Mukamel, S.; Garavelli, M. Bidimensional Electronic Spectroscopy on Indole in Gas Phase and in Water from First Principles. *Computational and Theoretical Chemistry* **2014**, *1040–1041*, 295–303. https://doi.org/10.1016/j.comptc.2014.03.031.
(105) Nenov, A.; a Beccara, S.; Rivalta, I.; Cerullo, G.; Mukamel, S.; Garavelli, M. Tracking Conformational Dynamics of Polypeptides by Nonlinear Electronic Spectroscopy of Aromatic Residues: A First-Principles Simulation Study. *ChemPhysChem* **2014**, *15* (15), 3282–3290. https://doi.org/10.1002/cphc.201402374.
(106) Nenov, A.; Mukamel, S.; Garavelli, M.; Rivalta, I. Two-Dimensional Electronic Spectroscopy of Benzene, Phenol, and Their Dimer: An Efficient First-Principles Simulation Protocol. *J. Chem. Theory Comput.* **2015**, *11* (8), 3755–3771. https://doi.org/10.1021/acs.jctc.5b00443.
(107) Polli, D.; Rivalta, I.; Nenov, A.; Weingart, O.; Garavelli, M.; Cerullo, G. Tracking the Primary Photoconversion Events in Rhodopsins by Ultrafast Optical Spectroscopy. *Photochem. Photobiol. Sci.* **2015**, *14* (2), 213–228. https://doi.org/10.1039/C4PP00370E.
(108) Rivalta, I.; Nenov, A.; Weingart, O.; Cerullo, G.; Garavelli, M.; Mukamel, S. Modelling Time-Resolved Two-Dimensional Electronic Spectroscopy of the Primary Photoisomerization Event in Rhodopsin. *J. Phys. Chem. B* **2014**, *118* (28), 8396–8405. https://doi.org/10.1021/jp502538m.

(109) Rivalta, I.; Nenov, A.; Garavelli, M. Modelling Retinal Chromophores Photoisomerization: From Minimal Models in Vacuo to Ultimate Bidimensional Spectroscopy in Rhodopsins. *Phys. Chem. Chem. Phys.* **2014**, *16* (32), 16865–16879. https://doi.org/10.1039/C3CP55211J.
(110) Loos, P.-F.; Boggio-Pasqua, M.; Scemama, A.; Caffarel, M.; Jacquemin, D. Reference Energies for Double Excitations. *J. Chem. Theory Comput.* **2019**, *15* (3), 1939–1956. https://doi.org/10.1021/acs.jctc.8b01205.
(111) Jaiswal, V. K.; Segarra-Martí, J.; Marazzi, M.; Zvereva, E.; Assfeld, X.; Monari, A.; Garavelli, M.; Rivalta, I. First-Principles Characterization of the Singlet Excited State Manifold in DNA/RNA Nucleobases. *Phys. Chem. Chem. Phys.* **2020**, *22* (27), 15496–15508. https://doi.org/10.1039/D0CP01823F.
(112) Pepino, A. J.; Segarra-Martí, J.; Nenov, A.; Improta, R.; Garavelli, M. Resolving Ultrafast Photoinduced Deactivations in Water-Solvated Pyrimidine Nucleosides. *J. Phys. Chem. Lett.* **2017**, *8* (8), 1777–1783. https://doi.org/10.1021/acs.jpclett.7b00316.
(113) Pepino, A. J.; Segarra-Martí, J.; Nenov, A.; Rivalta, I.; Improta, R.; Garavelli, M. UV-Induced Long-Lived Decays in Solvated Pyrimidine Nucleosides Resolved at the MS-CASPT2/MM Level. *Phys. Chem. Chem. Phys.* **2018**, *20* (10), 6877–6890. https://doi.org/10.1039/C7CP08235E.
(114) Brister, M. M.; Crespo-Hernández, C. E. Excited-State Dynamics in the RNA Nucleotide Uridine 5′-Monophosphate Investigated Using Femtosecond Broadband Transient Absorption Spectroscopy. *J. Phys. Chem. Lett.* **2019**, *10* (9), 2156–2161. https://doi.org/10.1021/acs.jpclett.9b00492.
(115) Segarra-Martí, J.; Nouri, S. M.; Bearpark, M. J. Modelling Photoionisations in Tautomeric DNA Nucleobase Derivatives 7H-Adenine and 7H-Guanine: Ultrafast Decay and Photostability. *Photochem* **2021**, *1* (2), 287–301. https://doi.org/10.3390/photochem1020018.
(116) Segarra-Martí, J.; Bearpark, M. J. Modelling Photoionisation in Isocytosine: Potential Formation of Longer-Lived Excited State Cations in Its Keto Form. *ChemPhysChem* **2021**, *22* (21), 2140–2140. https://doi.org/10.1002/cphc.202100733.
(117) Segarra-Martí, J.; Tran, T.; Bearpark, M. J. Computing the Ultrafast and Radiationless Electronic Excited State Decay of Cytosine and 5-methyl-cytosine Cations: Uncovering the Role of Dynamic Electron Correlation. *ChemPhotoChem* **2019**, *3* (9), 856–865. https://doi.org/10.1002/cptc.201900105.
(118) Segarra-Martí, J.; Tran, T.; Bearpark, M. J. Ultrafast and Radiationless Electronic Excited State Decay of Uracil and Thymine Cations: Computing the Effects of Dynamic Electron Correlation. *Phys. Chem. Chem. Phys.* **2019**, *21* (26), 14322–14330. https://doi.org/10.1039/C8CP07189F.
(119) Segarra-Martí, J.; Coto, P. B. A Theoretical Study of the Intramolecular Charge Transfer in 4-(Dimethylamino)Benzethyne. *Phys. Chem. Chem. Phys.* **2014**, *16* (46), 25642–25648. https://doi.org/10.1039/C4CP03436H.
(120) Krebs, N.; Pugliesi, I.; Hauer, J.; Riedle, E. Two-Dimensional Fourier Transform Spectroscopy in the Ultraviolet with Sub-20 Fs Pump Pulses and 250–720 Nm Supercontinuum Probe. *New J. Phys.* **2013**, *15* (8), 085016. https://doi.org/10.1088/1367-2630/15/8/085016.

(121) Borrego-Varillas, R.; Teles-Ferreira, D. C.; Nenov, A.; Conti, I.; Ganzer, L.; Manzoni, C.; Garavelli, M.; Maria de Paula, A.; Cerullo, G. Observation of the Sub-100 Femtosecond Population of a Dark State in a Thiobase Mediating Intersystem Crossing. *J. Am. Chem. Soc.* **2018**, *140* (47), 16087–16093. https://doi.org/10.1021/jacs.8b07057.
(122) Borrego-Varillas, R.; Nenov, A.; Kabaciński, P.; Conti, I.; Ganzer, L.; Oriana, A.; Jaiswal, V. K.; Delfino, I.; Weingart, O.; Manzoni, C.; Rivalta, I.; Garavelli, M.; Cerullo, G. Tracking Excited State Decay Mechanisms of Pyrimidine Nucleosides in Real Time. *Nat Commun* **2021**, *12* (1), 7285. https://doi.org/10.1038/s41467-021-27535-7.
(123) Marazzi, M.; Mai, S.; Roca-Sanjuán, D.; Delcey, M. G.; Lindh, R.; González, L.; Monari, A. Benzophenone Ultrafast Triplet Population: Revisiting the Kinetic Model by Surface-Hopping Dynamics. *J. Phys. Chem. Lett.* **2016**, *7* (4), 622–626. https://doi.org/10.1021/acs.jpclett.5b02792.
(124) Polli, D.; Altoè, P.; Weingart, O.; Spillane, K. M.; Manzoni, C.; Brida, D.; Tomasello, G.; Orlandi, G.; Kukura, P.; Mathies, R. A.; Garavelli, M.; Cerullo, G. Conical Intersection Dynamics of the Primary Photoisomerization Event in Vision. *Nature* **2010**, *467* (7314), 440–443. https://doi.org/10.1038/nature09346.
(125) Penfold, T. J.; Karlsson, S.; Capano, G.; Lima, F. A.; Rittmann, J.; Reinhard, M.; Rittmann-Frank, M. H.; Braem, O.; Baranoff, E.; Abela, R.; Tavernelli, I.; Rothlisberger, U.; Milne, C. J.; Chergui, M. Solvent-Induced Luminescence Quenching: Static and Time-Resolved X-Ray Absorption Spectroscopy of a Copper(I) Phenanthroline Complex. *J. Phys. Chem. A* **2013**, *117* (22), 4591–4601. https://doi.org/10.1021/jp403751m.
(126) Rankine, C. D.; Penfold, T. J. Progress in the Theory of X-Ray Spectroscopy: From Quantum Chemistry to Machine Learning and Ultrafast Dynamics. *J. Phys. Chem. A* **2021**, *125* (20), 4276–4293. https://doi.org/10.1021/acs.jpca.0c11267.